

Final Report

to

Air Force Office of Scientific Research (AFOSR)

for the project entitled

**“An Innovative Turbine Blade Cooling Technology & Micro/Miniature
Heat Pipes for Turbine Blades”**

Under contract

AFOSR-F49620-96-1-0315

Submitted by

Yiding Cao

Principal Investigator

Department of Mechanical Engineering
Florida International University
Miami, Florida 33199

20000906 015

Approved for public release;
distribution unlimited.

REPORT DOCUMENTATION PAGE

AFRL-SR-BL-TR-00-

0429

The public reporting burden for this collection of information is estimated to average 1 hour per response, including gathering and maintaining the data needed, and completing and reviewing the collection of information. Send comments of information, including suggestions for reducing the burden, to Department of Defense, Washington Headquarters (0704-0188), 1215 Jefferson Davis Highway, Suite 1204, Arlington, VA 22202-4302. Respondents should be aware that subject to any penalty for failing to comply with a collection of information if it does not display a currently valid OMB number.

PLEASE DO NOT RETURN YOUR FORM TO THE ABOVE ADDRESS.

1. REPORT DATE (DD-MM-YYYY) 15-07-00		2. REPORT TYPE Final		3. DATES COVERED (From - To) 06/96-06/99	
4. TITLE AND SUBTITLE An Innovative Turbine Blade Cooling Technology and Micro/Minature Heat Pipes for Turbine Blades				5a. CONTRACT NUMBER F49620-96-1-0315	
				5b. GRANT NUMBER AFOSR-F49620-96-1-0315	
				5c. PROGRAM ELEMENT NUMBER	
				5d. PROJECT NUMBER	
6. AUTHOR(S) Yiding Cao				5e. TASK NUMBER	
				5f. WORK UNIT NUMBER	
7. PERFORMING ORGANIZATION NAME(S) AND ADDRESS(ES) Florida International University, ME Department Miami, Florida 33199				8. PERFORMING ORGANIZATION REPORT NUMBER	
9. SPONSORING/MONITORING AGENCY NAME(S) AND ADDRESS(ES) Airforce Office of Scientific Research AFOSR/NA 110 Duncan Avenue, Suite B115 Bolling AFB, DC 20332-8080				10. SPONSOR/MONITOR'S ACRONYM(S) AFOSR	
				11. SPONSOR/MONITOR'S REPORT NUMBER(S)	
12. DISTRIBUTION/AVAILABILITY STATEMENT Approved for public release; distribution unlimited.					
13. SUPPLEMENTARY NOTES					
14. ABSTRACT Radially rotating miniature heat pipes for turbine blade cooling are studied by employing appropriate flow and heat transfer modeling as well as experimental tests. Extensive experimental tests on the heat pipes with different influential parameters are undertaken under a constructed high-speed rotating apparatus, and various effects of these parameters on the heat pipe performance are searched. Comprehensive analytical solutions for the heat pipe performance are also obtained, which are in very good agreement with the experimental data.					
15. SUBJECT TERMS Gas turbine blades, heat pipes, heat transfer and fluid flow					
16. SECURITY CLASSIFICATION OF:			17. LIMITATION OF ABSTRACT	18. NUMBER OF PAGES 109	19a. NAME OF RESPONSIBLE PERSON
a. REPORT	b. ABSTRACT	c. THIS PAGE			19b. TELEPHONE NUMBER (Include area code)

TABLE OF CONTENTS

LIST OF FIGURES	IV
LIST OF TABLES	VII
NOMENCLATURE	VIII
 1. INTRODUCTION	 1
1.1 Development of Gas Turbine Blade Cooling	1
1.2 Application Backgrounds and Working Principles of Radially Rotating Miniature Heat Pipes.....	8
 2. ANALYSES OF RADIALLY ROTATING MINIATURE HEAT PIPE PERFORMANCES	 13
2.1 Analytical Solution for the Liquid Film Distribution at the Condenser Section ..	13
2.2 General Solution for the Liquid Film Distribution at the Condenser Section with a Tilt Angle	21
2.3 Axial Vapor Flow Analyses along the Heat Pipe Length	28
2.4 Analytical Results for the Temperature Drop and Heat Transfer Limitations	35
 3. TEMPERATURE DISTRIBUTIONS ALONG THE HEAT PIPE LENGTH AND DIFFUSE EFFECTS OF NON-CONDENSABLE GASES	 47
3.1 Analysis of Vapor Temperature Distribution along the Heat Pipe	47
3.2 Analytical Solution of Temperature Distribution along the Heat Pipe Length Including the Effect of Non-Condensable Gases	50
 4. HIGH SPEED ROTATING TEST APPARATUS AND EXPERIMENTAL PROCEDURES	 58
4.1 High Speed Rotating Test Apparatus and Radially Rotating Miniature Heat Pipes	58
4.2 Experimental Results and Analyses	67
4.2.1 Operating and Startup Characteristics of High-Temperature Radially Rotating Miniature Heat Pipes	68

4.2.2 Effects of Heat Inputs	77
4.2.3 Effects of Cooling Air Flow Rates	81
4.2.4 Effects of Dimensionless Centrifugal Forces	85
4.2.5 Effects of Inner Diameters of Heat Pipes	89
4.3 Comparisons of the Theoretical Predictions and Experimental Data for the Temperature Distributions along the Heat Pipe Length	92
4.4 Error Analyses for the Temperature Distributions along the Heat Pipe Length	101
5. CONCLUSIONS AND RECOMMENDATIONS	104
5.1 Conclusions.....	104
5.2 Recommendations.....	108
6. REFERENCES	109

LIST OF FIGURES

1.1 Schematic of air convection cooling for turboengine blades	4
1.2 Schematic of air film cooling for the turboengine blades	5
1.3 Schematic of transpiration air cooling for the turboengine blades	6
1.4 Schematic of radially rotating heat pipe cooling for the turboengine blades	7
1.5 Schematic of air convection cooling combined with radially rotating heat pipe cooling for turboengine blades	10
1.6 Schematic of a radially rotating heat pipe with a tilt angle	11
1.7 Schematic of radially rotating heat pipe cooling for a turboengine disc	12
2.1 Schematic of a radially rotating heat pipe.....	18
2.2 Schematic of a differential control volume in the condensate liquid film	19
2.3 Schematic of a control volume at the liquid-vapor interface	20
2.4 Schematic of a differential control volume of condensate liquid film	27
2.5 Schematic of a thermal balance for the vapor flow in the condenser section	33
2.6 Schematic of an overall thermal balance in the condenser section	34
2.7 Maximum temperature drops across the liquid film for sodium as the working fluid ($T_v=1000$ K, $Q=200$ W).....	40
2.8 Maximum temperature drops across the liquid film for sodium as the working fluid ($D_h / L=0.025$, $Q=200$ W).....	41
2.9 Vapor temperature drops along the heat pipe length at different rotating speeds ($D_h / L=0.025$, $Q=200$ W).....	42
2.10 Vapor temperature drops along the heat pipe length at different heat pipe	

dimensionless sizes ($Q=200$ W, $\omega^2 \bar{Z}_a / g = 6.26 \times 10^4$).....	43
2.11 Vapor temperature drops along the heat pipe length at different heat input ($D_h / L = 0.025$, $\omega^2 \bar{Z}_a / g = 3.91 \times 10^3$).....	44
2.12 Ratio of the vapor temperature drops due to the centrifugal force to the total temperature drop ($T_v = 1000$ K, $Q = 200$ W).....	45
2.13 Entrainment limitations as a function of rotating speeds ($T_{ref} = 937$ K for potassium and $T_{ref} = 1073$ K for sodium).....	46
3.1 Schematic of diffuse effects of non-condensable gases in the condenser section.....	57
4.1 Schematic of a high-speed rotating test apparatus and data acquisition system.....	63
4.2 Schematic of a high-speed rotating apparatus.....	64
4.3 Schematic of a radially rotating miniature heat pipe with an inner diameter of 1.5 mm	65
4.4 Schematic of a radially rotating miniature heat pipe with an inner diameter of 2 mm.....	66
4.5 Comparisons of temperature distributions and heat inputs between the heat pipe and the heat pipe container.....	73
4.6 Temperature distributions along the dimensionless heat pipe length with the diffuse effects of non-condensable gases during the heat pipe startup process.....	75
4.7 Temperature distributions along the dimensionless heat pipe length with different heat inputs.....	76
4.8 Temperature distributions along the dimensionless heat pipe length with different rotating frequencies and flow rates of cooling air.....	79
4.9 Temperature distributions along the dimensionless heat pipe length with different rotating frequencies and flow rates of cooling air.....	80
4.10 Comparisons of temperature distributions along the dimensionless heat pipe length with different flow rates of cooling air.....	83
4.11 Comparisons of temperature distributions along the dimensionless heat pipe length with different flow rates of cooling air.....	84

4.12 Temperature distributions along the heat pipe with different rotating frequencies and flow rates of cooling air.....	87
4.13 Temperature distributions along the dimensionless heat pipe length with different rotating frequencies and flow rates of cooling air.....	88
4.14 Comparisons of temperature distributions along the dimensionless heat pipe length.....	90
4.15 Comparisons of temperature distributions along the dimensionless heat pipe length.....	91
4.16 Comparisons of analytical solutions, experimental results and analytical solutions with the diffuse effects of non-condensable gases in the heat pipe ($L_{c,n}=4\text{ mm}$)...	97
4.17 Schematic of the diffuse effects of non-condensable gases at a higher revolution..	100

LIST OF TABLES

4.1 Comparisons of the temperature distributions for the heat pipe and heat pipe container with the same geometry.....	72
4.2 Temperature distributions along the heat pipe length with the diffuse effects of non-condensable gases during the heat pipe startup process.....	74
4.3 Comparisons of analytical solutions, experimental results, and analytical solutions with the diffuse effects of non-condensable gases in the heat pipe ($L_{c,n} = 4 \text{ mm}$).....	95

LIST OF SYMBOLS

A	cross-sectional area, m^2
Bo	Bond number
C_w	empirical constant in Wallis' correlation
D	heat pipe diameter, m
F_v	frictional coefficient
f	skin-friction coefficient or rotating frequency, Hz
g	gravitational acceleration, m/s^2
h_c	heat transfer coefficient, $\text{W/m}^2\text{K}$
h_{fg}	latent heat of vaporization, J/kg
k	thermal conductivity, W/mK
k_p	thermal conductivity of heat pipe wall, W/m-K
L	length of the heat pipe, m
L_a	adiabatic length, m
L_c	condenser length, m
L_e	evaporator length, m
L_{eff}	effective length of the heat pipe, m
$L_{c,n}$	length of the heat pipe occupied by the non-condensable gas, m
m	coefficient, $1/\text{m}$
\dot{m}	mass flow rate, kg/s
M_v	Mach number
p	pressure, N/m^2
Q	heat transfer rate, W
q''	heat flux, W/m^2
Re	Reynolds number
R	heat pipe radius, m
T	temperature, K or $^{\circ}\text{C}$

w	axial velocity, m/s
W	flow rate of cooling air, m ³ /s
x	axial coordinate, m
z	axial location of the heat pipe, m
Z	revolving radius of the heat pipe, m
ϕ	tilt angle between the heat pipe centerline and the disk radial line, degree
θ	rotating angle of the heat pipe, degree
Γ	liquid mass flow rate per unit circumferential length, kg/m-s
δ	thickness of liquid film, m
σ	surface tension, N/m
ρ	density, kg/m ³
μ	dynamic viscosity, kg/m-s
τ	shear stress, N/m ²
ω	angular velocity, rad/s
ψ	dimensionless coefficient

Subscripts

a	adiabatic section or average
c	condenser
e	evaporator
ent	entrainment
eff	effective
l	liquid phase
p	heat pipe wall
v	vapor phase
z	axiial location of the heat pipe
$R-\delta$	liquid-vapor interface

1. INTRODUCTION

1.1 Development of Gas Turbine Blade Cooling

Aerospace turboengines present a demanding challenge to many heat transfer scientists and engineers. Designers in the field are always seeking the best design to transform the chemical energy of the fuel into the useful work of propulsive thrust at maximum effectiveness (D. G. Shepherd, 1972, J. H. Horlock, 1985). Based on the principles of thermodynamics, the inlet temperature and pressure of the gas in aerospace turboengines must be increased in order to improve the thermal efficiency of the turboengines. As a result, advanced gas turbines are designed to work at a inlet temperature of 1500-1700 K, and the turbine blades must operate at very hostile environments. This hostile working condition is often in conflict with the material capability of withstanding these high temperatures (E. R. Norster, 1969).

Turbine blade cooling was first considered in a German design in 1935. It presented a very tough but important problem to heat transfer researchers and scientists due to the high temperature and rotation of turbine blades (Bathie, 1984, Cohen, 1987).

There are basically three approaches considered by the thermal engineer worldwide to solve these problems. The first approach is to develop a new surface coating that can withstand these hostile environments and has a very low heat conductivity to protect the blade surface. This approach is very practical and valuable. However, the progress in this approach is generally slow. Because this new surface coating must be subject to the impingement of high temperature gas and the vibration of turboengines, the new surface coating is difficult to attach onto the blade surface firmly.

The second approach is the air cooling technology that is the primary method used in the blade cooling so far. The air cooling technology is a traditional, convenient, and effective blade cooling means. It is subdivided into the following three kinds:

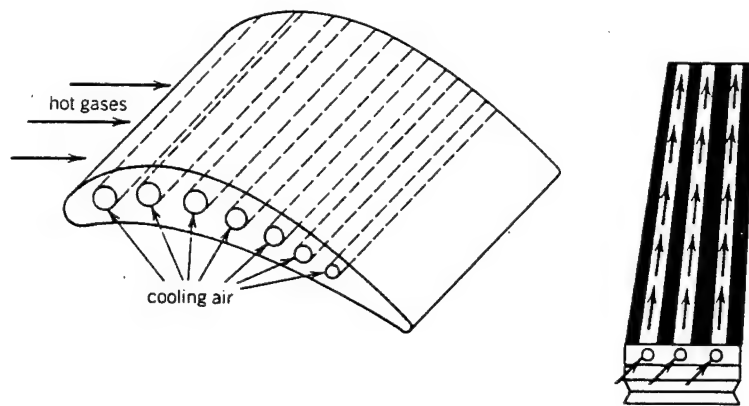
(1) Convection cooling, which is an early blade cooling means. Cooling air from the compressor flows into the inner channels in the blade from the blade root, and flows out from the blade top. The spent air is discharged and mixed with the main gas flow of the next stage. Because the heat stored in the blades can be carried away through the cooling air convection, the blades can be cooled effectively, as shown in Fig. 1.1a. But due to the narrow space of the cooling passage at the blade trailing edge, the flow resistance to the cooling air will be increased, and flow rate of the cooling air will be reduced there accordingly. As a result, the air cooling effect at the trailing edge will be decreased, and the temperature at the trailing edge will be substantially higher than that of other regions in the blade, as shown in Fig. 1.1b.

(2) Film cooling, in which the cooling air not only passes through the inner channels in the blade, but also flows out from the blade surface and trailing edge. Air film cooling involves the injection of cooling air into the boundary layer of high temperature gas on the blade surfaces, as shown in Fig. 1.2. Therefore, it provides a protective layer to the blade surfaces. At the same time, the temperature gradient in the cross-sectional area of the blade will be decreased greatly. But the air film cooling not only needs a lot of cooling air, but also adversely affects the aerodynamic and thermodynamic performance of the aerospace turboengines. For example, a turbine stage with the film cooling would have an thermal efficiency of about 85%. But for a turbine stage without the film cooling,

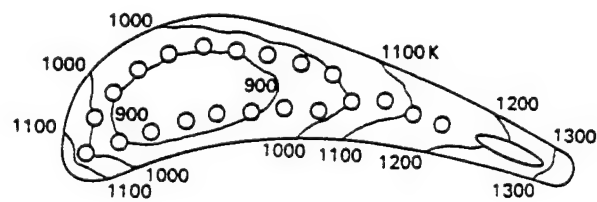
the thermal efficiency would be about 90%. Therefore, the loss in thermal efficiency is substantial.

(3) Air transpiration cooling or porous cooling, which involves the use of porous material. The cooling air in this case is forced into the blade surfaces to form a relatively cool insulating film, as shown in Fig. 1.3. It is an effective cooling method for the blade, but it is easy to lead to pore blockage due to material oxidation. It would also cause the blade break because of the high revolution and vibration of turboengines.

The third approach for the blade cooling is the heat pipe cooling technology which provides a potentially effective cooling means for the structure exposed to high heat fluxes. Because heat pipes have operational characteristics of having a very high effective thermal conductance, and the ability to act as a thermal flux transformer to create an isothermal surface of low thermal impedance, they can be employed in the turbine blades as a cooling device, as shown in Fig. 1.4.

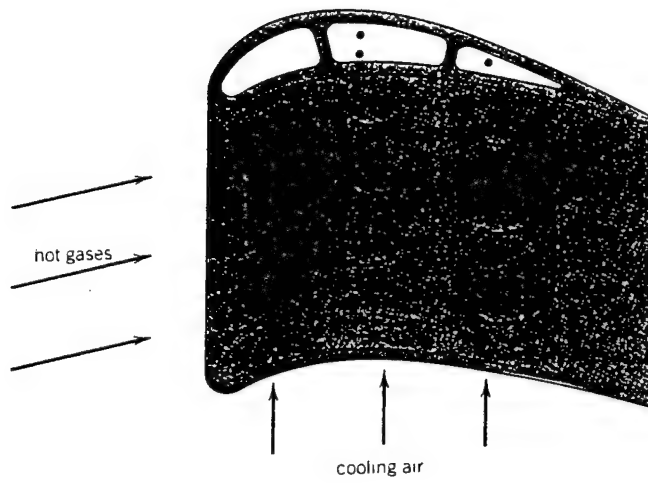


(a)



(b)

Fig. 1.1 Schematic of air convection cooling for turboengine blades. (Cohen, et. al, 1987)



(a)



(b)

Fig. 1.2 Schematic of air film cooling for turboengine blades. (Bathie, 1984)

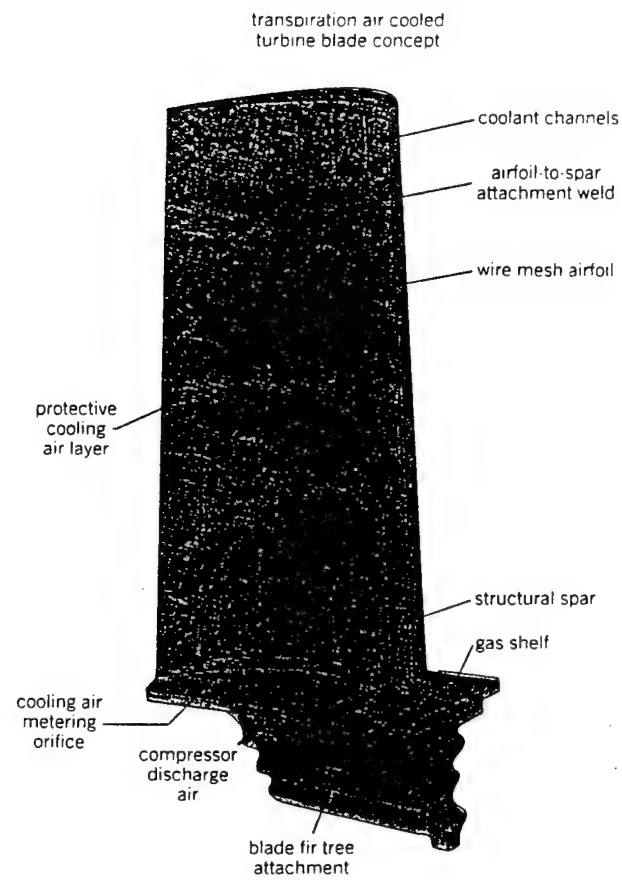


Fig. 1.3 Schematic of transpiration air cooling for turboengine blades. (Bathie, 1984)

Radially Rotating Heat Pipes

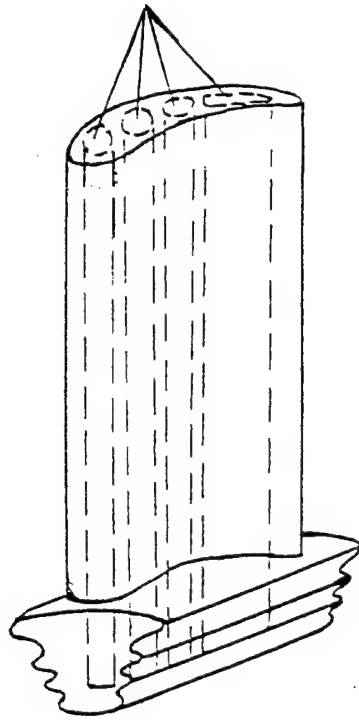


Fig. 1.4 Schematic of radially rotating heat pipe cooling for turboengine blades.

1.2 Application Backgrounds and Working Principles of Radially Rotating

Miniature Heat Pipes

Gas turbine blade cooling is crucial for a higher combustion temperature and consequently a higher engine thermal efficiency. Air cooling technology is more convenient and effective, but the coolant flow in the blades affects not only the heat transfer but also the aerodynamic and thermodynamic performance of the aerospace turboengines. At the same time, there are some other problems associated with the air cooling.

1) Air cooling effectiveness is reduced towards the blade tip as it picks up heat. The result will be the rise of the general level of blade temperature from the bottom to the tip. Therefore, it will result in a large temperature gradient between the blade bottom and the tip.

2) Because of the narrow space of blade trailing edge, the flow resistance of the cooling air will be increased, and flow rate of cooling air will be reduced there. The temperature gradient over the cross-section area of the blade will be increased, as shown in Fig. 1.1b.

3) Air cooling technology needs about 2% of the total cooling air flow from the compressor to cool the high temperature components, so this will result in a reduction in the efficiency of the gas turbine equipment.

In order to reduce the temperature gradient in turbine blades and increase the cooling effectiveness, combining the air cooling technology with radially rotating miniature heat pipes for the blade cooling is an innovative approach. As mentioned earlier, there exists a large temperature gradient over the cross-sectional area of the blade

and between the tip and bottom of the blade. In order to solve this problem, a radially rotating miniature heat pipe can be installed in the blades, as shown in Fig. 1.5. The radially rotating heat pipe, which rotates about the axis of revolution, is a wickless heat pipe that is comprised of an air-evacuated hollow container and an amount of working fluid sealed within the container, as shown in the Fig. 1.6. The centrifugal force generated by the rotating motion of the heat pipe is utilized for the return of the liquid condensate from the condenser to the evaporator. The heat in the blades is transferred from the evaporator to the condenser, where the heat is carried away by the cooling air convection. Because the radially rotating miniature heat pipe has a very high thermal conductance, the temperature gradients over the cross-sectional area of the blade and between the tip and bottom of the blade will be reduced greatly under this new cooling approach.

In addition, the top portion of a turbine disk will operate in a high temperature condition because the blades of a gas turbine are directly attached to the disk. Therefore, the radially rotating heat pipe can be also applied in the disc cooling application, as shown in Fig. 1.7 (Cao, 1998).

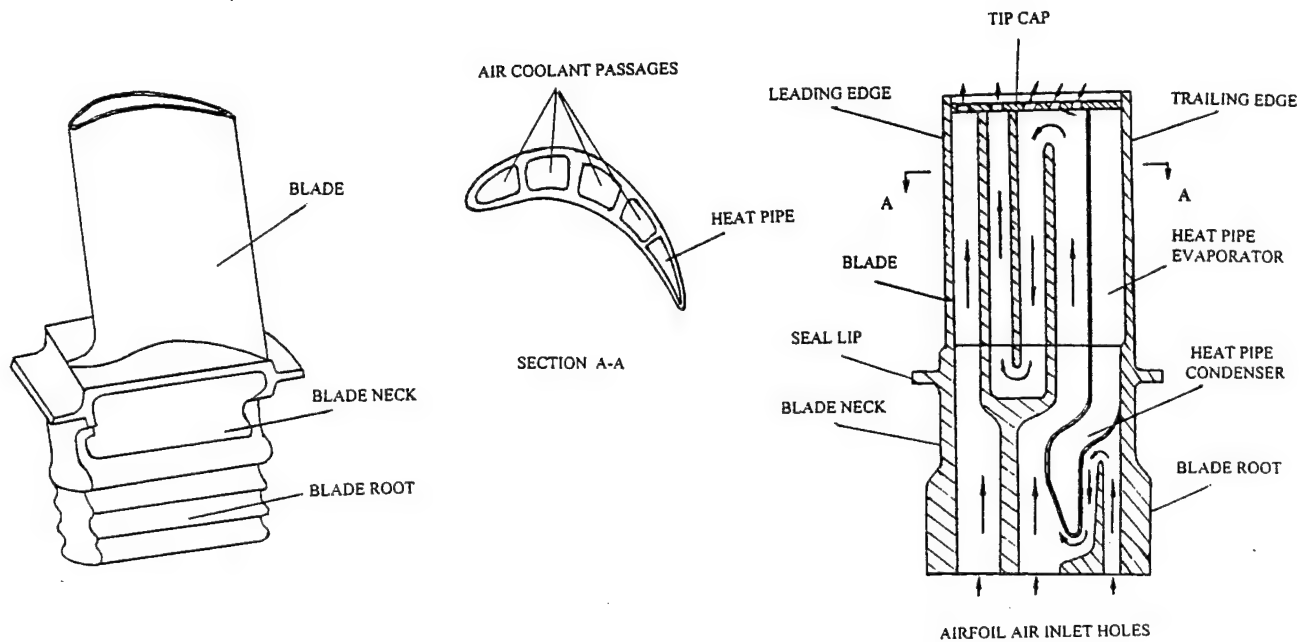


Fig. 1.5 Schematic of air convection cooling combined with radially rotating heat pipe cooling for turboengine blades.

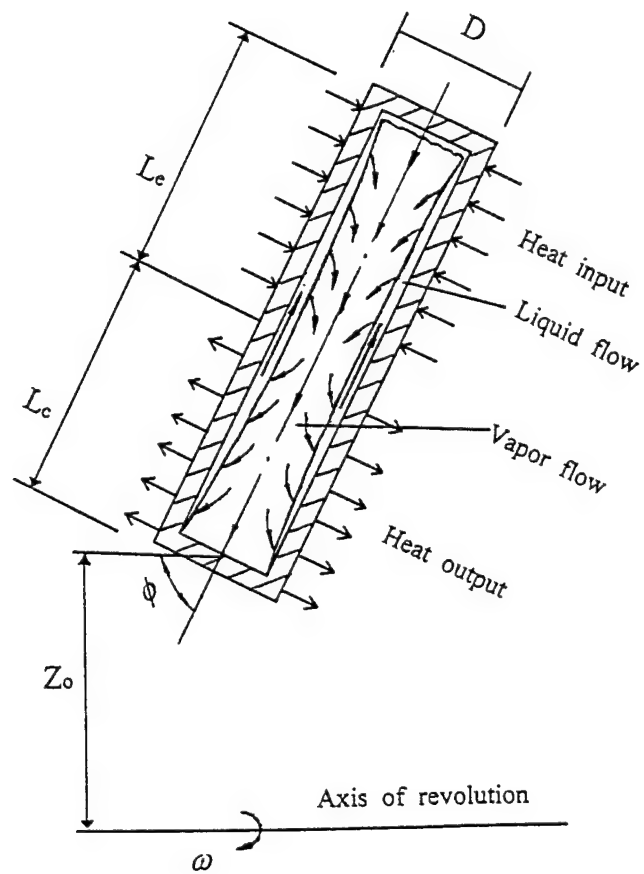


Fig. 1.6 Schematic of a radially rotating heat pipe with a tilt angle.

Radially Rotating Heat Pipes

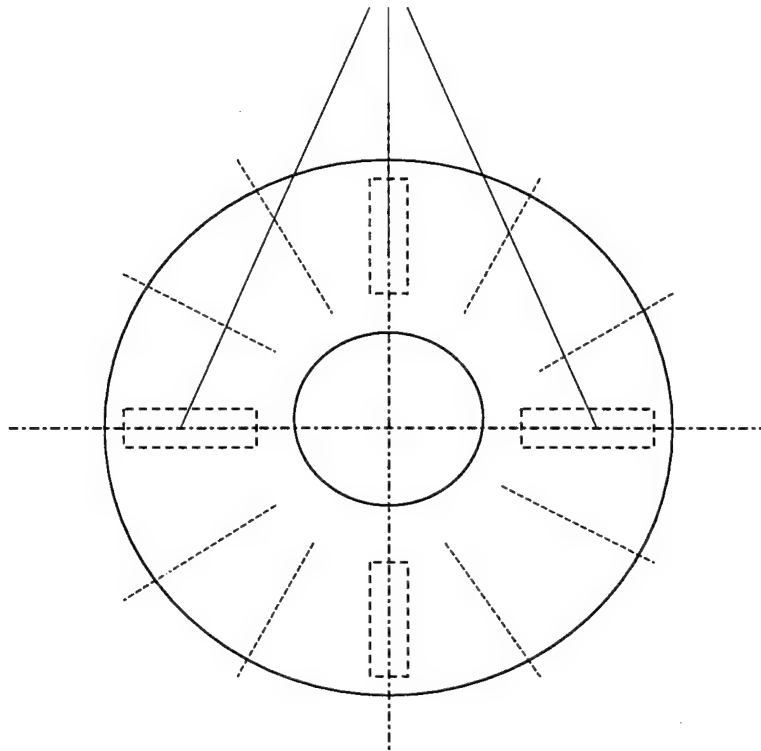


Fig. 1.7 Schematic of radially rotating heat pipe cooling for a turboengine disc.

2. ANALYSES OF RADially ROTATING MINIATURE HEAT PIPE PERFORMANCE

2.1 Analytical Solution for the Liquid Film Distribution in the Condenser Section

As mentioned in the previous chapter, a radially rotating heat pipe, which rotates about the axis of revolution, is a wickless heat pipe that is comprised of an air-evacuated hollow container and an amount of working fluid sealed within the container. Before the heat pipe is actually applied to the turbine blade, however, the fundamental transport phenomena related to various heat transfer limitations must be fully understood.

Fig. 2.1 schematically illustrates a radially rotating heat pipe and its interior working conditions. The assumptions of the general thin-film condensation analysis are as follows:

1. The vapor condensation is filmwise.
2. Liquid subcooling is negligible.
3. Convective effects in the liquid are negligible.
4. The liquid film thickness is much smaller than the vapor space radius.
5. Circumferential velocity and temperature gradients are negligible.
6. The vapor pressure over the cross-sectional area of the miniature heat pipe is uniform.
7. The thermocapillary flow effects are negligible in the presence of a large body force field.

However, since the size of the present heat pipe is very small, the curvature effect of the heat pipe wall on the liquid film distribution may be included. Therefore, a cylindrical

coordinate system is employed in the present study. For analyses, a cylindrical differential control volume in the liquid condensate film of a radially rotating heat pipe is schematically shown in Fig. 2.2, where the liquid centrifugal force and gravitational force are $f_c = 2\pi\rho_l\omega^2 Zrdrdz$ and $f_g = 2\pi\rho_l g r dr dz \cos\theta$, respectively. A static force balance in z direction results in the following differential equation:

$$p_{l,z} 2\pi r dr - (p_{l,z} + \frac{\partial p_{l,z}}{\partial z} dz) 2\pi r dr + \tau_{l,z} 2\pi r dr dz - (\tau_{l,r} + \frac{\partial \tau_{l,r}}{\partial r} dr) (2\pi r + dr) dz + \rho_l (\omega^2 Z - g \cos\theta) 2\pi r dr dz = 0 \quad (2.1)$$

where $Z \approx z_0 + z$ is the revolving radius of the control volume, θ is the rotating angle of heat pipe.

Since $r \gg dr$ and $2\pi r + dr \approx 2\pi r$, simplifying Eq. (2.1), we have

$$\frac{\partial \tau_{l,r}}{\partial r} + \frac{\partial p_{l,z}}{\partial z} - \rho_l (\omega^2 Z - g \cos\theta) = 0 \quad (2.2)$$

The static force balance in r direction is

$$p_{l,r} 2\pi r dz - (p_{l,r} + \frac{\partial p_{l,r}}{\partial r} dr) (2\pi r + dr) dz = 0 \quad (2.3)$$

Simplifying the equation by neglecting higher order infinitesimals,

$$\frac{\partial p_{l,r}}{\partial r} = 0 \quad (2.4)$$

Eq. (2.4) means that the pressure of the liquid film is a function of z only. The shear stress and pressure at the liquid film surface can be studied by considering the momentum equations in both z and r directions based on the interface control volume shown in Fig.2.3.

We get

$$\tau_{l,R-\delta} 2\pi r dz = -\tau_{v,R-\delta} 2\pi r dz - (\bar{w}_v + w_{l,R-\delta}) \frac{d\Gamma_l}{dz} 2\pi r dz \quad (2.5)$$

$$p_{v,R-\delta} 2\pi r dz - p_{l,R-\delta} (2\pi r + dr) dz + (\bar{w}_v + w_{l,R-\delta}) \frac{d\Gamma_l}{dz} 2\pi r dz = 0 \quad (2.6)$$

where Γ_l is the liquid mass flow rate per unit circumferential length, \bar{w}_v and $w_{l,R-\delta}$ are the average vapor velocity and liquid velocity at the liquid film surface, respectively. $\tau_{l,R-\delta}$ and $\tau_{v,R-\delta}$ are the shear stresses of the liquid film and vapor at the liquid-vapor interface due to the countercurrent liquid and vapor flows, and δ is the thickness of the thin liquid film, as shown in Fig. 2.3.

Because $\frac{d\Gamma_l}{dz}$ is very small and can be ignored, Eq. (2.5) and (2.6) can be simplified as follows:

$$\tau_{l,R-\delta} = -\tau_{v,R-\delta} \quad (2.7)$$

$$p_{l,R-\delta} = p_{v,R-\delta} \quad (2.8)$$

It is reasonable to assume that the vapor pressure over the cross section of the heat pipe is uniform since the cross-section area of miniature heat pipes is very small. According to Eqs. (2.4) and (2.8),

$$p_l(z) = p_v(z) \quad (2.9)$$

This means that the pressures of vapor and liquid in the r direction in the condenser section are the same, and vary only in z direction. Therefore, Eq. (2.2) can be rewritten as:

$$\frac{\partial \tau_{l,r}}{\partial r} + \frac{dp_v}{dz} - \rho_l(\omega^2 Z - g \cos \theta) = 0 \quad (2.10)$$

The boundary conditions for the above equation is

$$w_l = 0 \quad \text{at } r = R \quad (2.11)$$

$$\mu_l \frac{\partial w_l}{\partial r} = -\tau_{l,R-\delta} = \tau_{v,R-\delta} \quad \text{at } r = R - \delta \quad (2.12)$$

Integrating Eq. (2.10) along r direction yields the following expression:

$$-\tau_{l,r} = \frac{dp_v}{dz} r - \rho_l (\omega^2 Z - g \cos \theta) r + c_1 \quad (2.13)$$

For a Newtonian fluid,

$$\tau_{l,r} = -\mu_l \frac{dw_l}{dr} \quad (2.14)$$

Plugging Eq. (2.14) into Eq. (2.13) and integrating it along r direction again yield

$$w_l = \frac{1}{\mu_l} \left[\frac{dp_v}{dz} - \rho_l (\omega^2 Z - g \cos \theta) \right] \frac{r^2}{2} + \frac{c_1}{\mu_l} r + c_2 \quad (2.15)$$

According to boundary conditions (2.11) and (2.12), we have

$$w_l = \frac{1}{\mu_l} \left[\frac{1}{2} (R^2 - r^2) - (R - r)(R - \delta) \right] \left[\rho_l (\omega^2 Z - g \cos \theta) - \frac{dp_v}{dz} \right] - \frac{1}{\mu_l} \tau_{v,R-\delta} (R - r) \quad (2.16)$$

Once the velocity distribution is found, the liquid mass flow rate per unit circumferential length, Γ_l , is evaluated through the following integral:

$$\Gamma_l = \frac{m_l}{\pi D} = \frac{1}{2\pi R} \int_{R-\delta}^R \rho_l w_l 2\pi r dr \quad (2.17)$$

For the radially rotating heat pipe with a high speed, the liquid film thickness, δ , is much smaller than the heat pipe radius, R . Therefore, r and R are roughly equal and can be canceled in Eq. (2.17). Substituting Eq. (2.16) into Eq. (2.17) and integrating it yields

$$\Gamma_l \approx \frac{\rho_l}{\mu_l} \left[\rho_l (\omega^2 Z - g \cos \theta) - \frac{dp_v}{dz} \right] \frac{\delta^3}{3} - \frac{\rho_l}{\mu_l} \tau_{v,R-\delta} \frac{\delta^2}{2} \quad (2.18)$$

The following relation can also be used to evaluate the mass flow rate based on the energy balance by neglecting the change of sensible heat.

$$\Gamma_l = \int_0^z \frac{q_c''}{h_{fg}} dz = \frac{\bar{q}_c''}{h_{fg}} z \quad (2.19)$$

where q_c'' and \bar{q}_c'' are the heat flux and the average heat flux in the condenser section, respectively. Substituting Eq. (2.19) into Eq. (2.18) and recasting it, the solution for the liquid film thickness is found:

$$-\frac{\rho_l h_{fg}}{3\mu_l \bar{q}_c'' z} [\rho_l (\omega^2 Z - g \cos \theta) - \frac{dp_v}{dz}] \delta^3 + \frac{\rho_l h_{fg} \tau_{v,R-\delta}}{2\mu_l \bar{q}_c'' z} \delta^2 + 1 = 0 \quad (2.20)$$

Once the liquid film thickness is evaluated from Eq. (20), the temperature drop, ΔT_l , across the liquid film can be calculated

$$\Delta T_l = \frac{R \bar{q}_c'' \ln \frac{R}{R-\delta}}{k_l} \cong \frac{\bar{q}_c'' \delta}{k_l} \quad (2.21)$$

The local heat transfer coefficient, h_z , and local Nusselt number, Nu_z , in the condenser section are defined, respectively,

$$h_z = \frac{\bar{q}_c''}{\Delta T_l} \cong \frac{k_l}{\delta} \quad (2.22)$$

$$Nu_z = \frac{h_z z}{k_l} \cong \frac{z}{\delta} \quad (2.23)$$

where k_l is the heat conductivity of the liquid film.

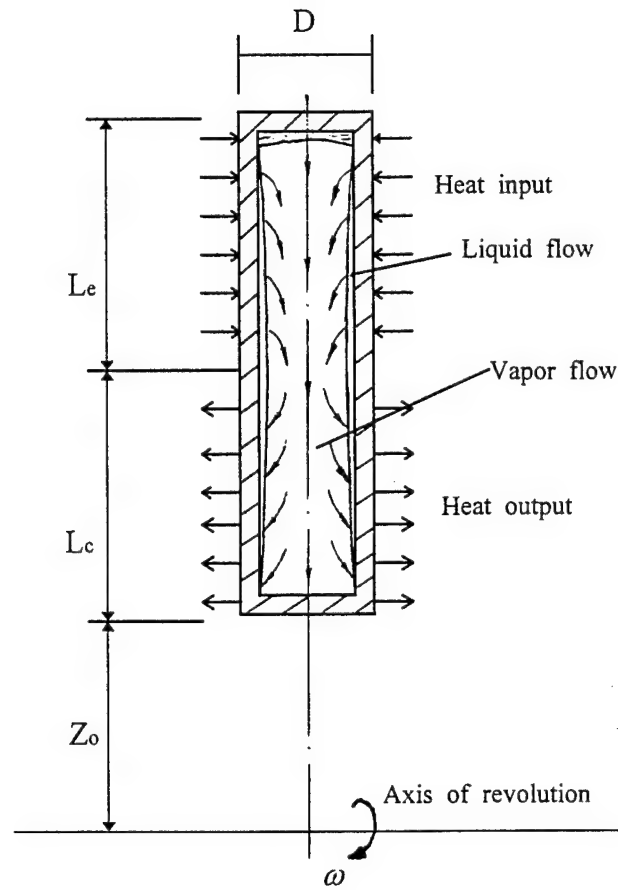


Fig. 2.1 Schematic of a radially rotating heat pipe.

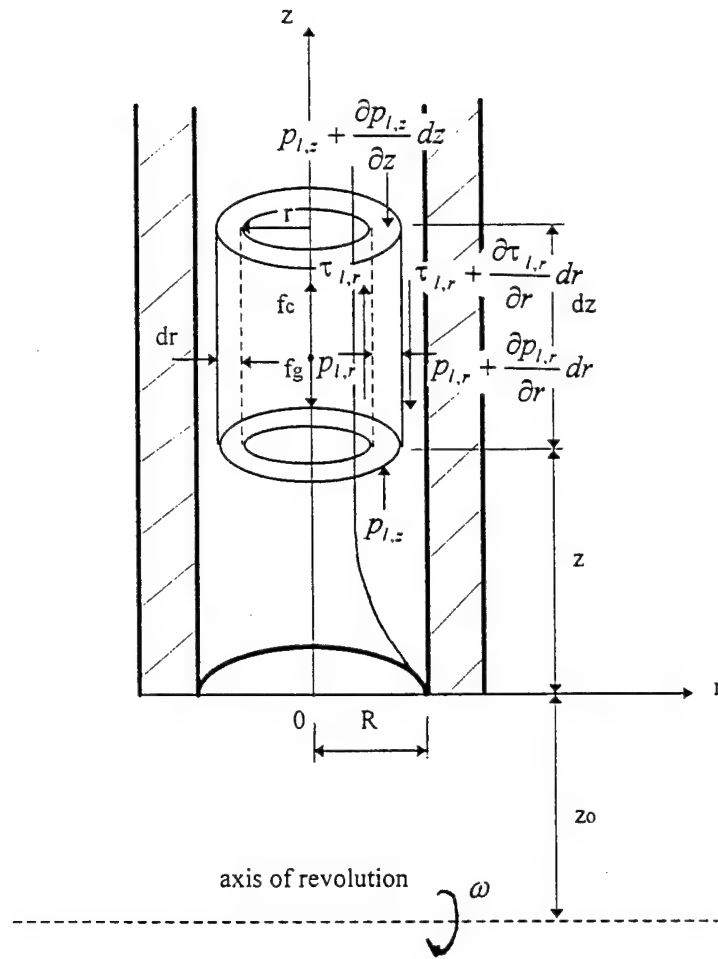


Fig. 2.2 Schematic of a differential control volume in the condensate film.

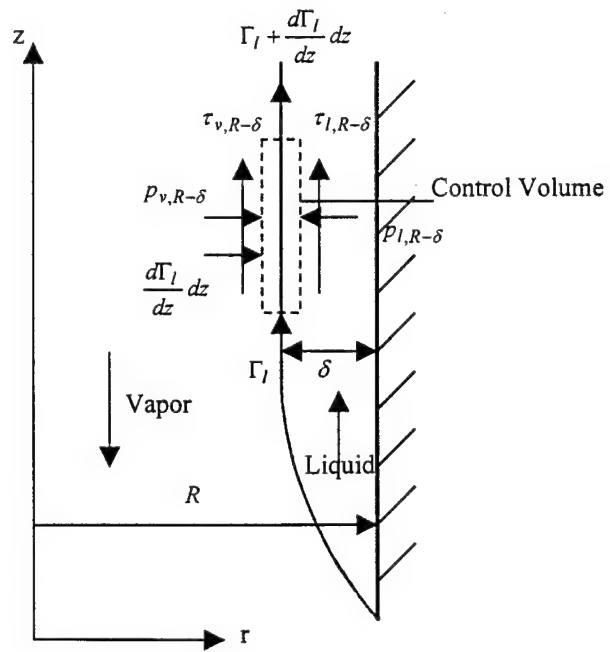


Fig. 2.3 Schematic of a control volume at the liquid-vapor interface.

2.2 General Solution for the Liquid Film Distribution in the Condenser Section with a Tilt Angle

The basic assumptions of the mathematical model are the same as those in chapter

2.1. In general, the tilt angle, ϕ , of the heat pipe should be close to 90° , as shown in Fig.

2.4. A static force balance in the z direction gives

$$\begin{aligned} p_l 2\pi r dr - (p_l + \frac{\partial p_l}{\partial z} dz) 2\pi r dr + \tau_l 2\pi r dz - 2\pi(r + dr) dz (\tau_l + \frac{\partial \tau_l}{\partial r} dr) \\ + \rho_l (\omega^2 \bar{Z} - g \cos \theta) \sin \phi 2\pi r dr dz = 0 \end{aligned} \quad (2.24)$$

where $\bar{Z} = z_0 + z \sin \phi$ is the revolving radius of the control volume, z_0 is the revolving radius of the coordinate origin.

Because $r \gg dr$,

$$2\pi(r + dr) dz = 2\pi r dz + 2\pi dr dz \approx 2\pi r dz \quad (2.25)$$

Plugging Eq. (2.25) in Eq. (2.24) yields

$$\begin{aligned} p_l 2\pi r dr - (p_l + \frac{\partial p_l}{\partial z} dz) 2\pi r dr + \tau_l 2\pi r dz - 2\pi r dz (\tau_l + \frac{\partial \tau_l}{\partial r} dr) \\ + \rho_l (\omega^2 \bar{Z} - g \cos \theta) \sin \phi 2\pi r dr dz = 0 \end{aligned} \quad (2.26)$$

Simplifying Eq. (2.26) and rearranging it

$$\frac{\partial \tau_l}{\partial r} = - \frac{\partial p_l}{\partial z} + \rho_l (\omega^2 \bar{Z} - g \cos \theta) \sin \phi \quad (2.27)$$

A static force balance in r direction would give

$$p_l 2\pi r dz - (p_l + \frac{\partial p_l}{\partial r} dr) 2\pi(r + dr) dz - \rho_l (\omega^2 \bar{Z} - g \cos \theta) \cos \phi 2\pi r dr dz = 0 \quad (2.28)$$

Eq. (2.28) can be simplified and recast as

$$\frac{\partial p_l}{\partial r} = -\rho_l(\omega^2 \bar{Z} - g \cos \theta) \cos \phi \quad (2.29)$$

Integrating Eq. (2.29) from r to $R - \delta$ yields

$$p_{l,R-\delta} - p_l = -\rho_l(\omega^2 \bar{Z} - g \cos \theta) \cos \phi (r - R + \delta) \quad (2.30)$$

$$\text{Therefore} \quad p_l = p_{l,R-\delta} + \rho_l(\omega^2 \bar{Z} - g \cos \theta) \cos \phi (r - R + \delta) \quad (2.31)$$

Differentiating Eq. (2.31) with respect to z gives

$$\frac{\partial p_l}{\partial z} = \frac{\partial p_{l,R-\delta}}{\partial z} + \rho_l \omega^2 \sin \phi \cos \phi (r - R + \delta) + \rho_l(\omega^2 \bar{Z} - g \cos \theta) \cos \phi \frac{d\delta}{dz} \quad (2.32)$$

Assuming that the liquid pressure at the liquid-vapor interface is equal to the vapor pressure, we have

$$p_{l,R-\delta} = p_v \quad (2.33)$$

Substituting Eq. (2.33) into Eq. (2.32) gives

$$\frac{\partial p_l}{\partial z} = \frac{\partial p_v}{\partial z} + \rho_l \omega^2 \sin \phi \cos \phi (r - R + \delta) + \rho_l(\omega^2 \bar{Z} - g \cos \theta) \cos \phi \frac{d\delta}{dz} \quad (2.34)$$

Plugging Eq. (2.34) into Eq. (2.27), we have

$$\frac{\partial \tau_l}{\partial r} = -\frac{\partial p_v}{\partial z} - \rho_l \omega^2 \sin \phi \cos \phi (r - R + \delta) + \rho_l(\omega^2 \bar{Z} - g \cos \theta) (\sin \phi - \cos \phi \frac{d\delta}{dz}) \quad (2.35)$$

since $\frac{d\delta}{dz}$ is very small,

$$\sin \phi - \cos \phi \frac{d\delta}{dz} \approx \sin \phi \quad (2.36)$$

Substituting Eq. (2.36) into Eq. (2.35) and integrating it yield

$$\tau_l = \left[-\frac{\partial p_v}{\partial z} r + \rho_l(\omega^2 \bar{Z} - g \cos \theta) \sin \phi \right] r - \rho_l \omega^2 \sin \phi \cos \phi \left[\frac{r^2}{2} - (R - \delta)r \right] + c_1 \quad (2.37)$$

Since $\tau_l = -\mu_l \frac{dw_l}{dr}$, replacing τ_l with this relation in Eq. (2.37) and integrating it,

$$w_l = \frac{1}{2\mu_l} \left[\frac{\partial p_v}{\partial z} - \rho_l (\omega^2 \bar{Z} - g \cos \theta) \sin \phi \right] r^2 + \frac{\rho_l}{\mu_l} \omega^2 \sin \phi \cos \phi \left[\frac{r^3}{6} - \frac{1}{2} (R - \delta) r^2 \right] - \frac{c_1}{\mu_l} r + c_2 \quad (2.38)$$

The two constants in the above equation can be determined by the following two boundary conditions:

$$w_l = 0 \quad \text{at } r = R \quad (2.39)$$

$$\tau_{l,R-\delta} = -\tau_{v,R-\delta} - (\bar{w}_v + w_{l,R-\delta}) \frac{d\Gamma_l}{dz} \quad \text{at } r = R - \delta \quad (2.40)$$

Since $\frac{d\Gamma_l}{dz}$ is very small and negligible, Eq. (2.40) can be simplified as

$$\tau_{l,R-\delta} = -\tau_{v,R-\delta} \quad \text{at } r = R - \delta \quad (2.41)$$

After determining the two constants in Eq. (2.38) based on two boundary conditions, the velocity of liquid in z direction is obtained

$$w_l = \frac{1}{\mu_l} \left[\frac{\partial p_v}{\partial z} - \rho_l (\omega^2 \bar{Z} - g \cos \theta) \sin \phi \right] \left[(R - \delta)(R - r) - \frac{1}{2} (R^2 - r^2) \right] - \frac{1}{\mu_l} \tau_{v,R-\delta} (R - r) - \frac{\rho_l}{\mu_l} \omega^2 \sin \phi \cos \phi \left[\frac{1}{2} (R - \delta)^2 (R - r) - \frac{1}{2} (R - \delta)(R^2 - r^2) + \frac{1}{6} (R^3 - r^3) \right] \quad (2.42)$$

The liquid mass flow rate per unit circumferential length, Γ_l , is

$$\begin{aligned} \Gamma_l &= \frac{\dot{m}_l}{\pi D} = \frac{1}{2\pi R} \int_{R-\delta}^R \rho_l w_l 2\pi r dr \\ &= \frac{\rho_l}{\mu_l R} \left\{ \left[\frac{\partial p_v}{\partial z} - \rho_l (\omega^2 \bar{Z} - g \cos \theta) \sin \phi \right] \left(-\frac{1}{3} R \delta^3 + \frac{5}{24} \delta^4 \right) - \tau_{v,R-\delta} \left(\frac{1}{2} R \delta^2 - \frac{1}{3} \delta^3 \right) \right\} \end{aligned}$$

$$- \rho_l \omega^2 \sin \phi \cos \phi \left(\frac{1}{8} R \delta^4 - \frac{3}{40} \delta^5 \right) \quad (2.43)$$

According to the energy balance, Γ_l can also be evaluated by the following relation

$$\Gamma_l = \int_0^z \frac{\bar{q}_c}{h_{fg}} dz = \frac{\bar{q}_c}{h_{fg}} z \quad (2.44)$$

Substituting Eq. (2.44) into Eq. (2.43) gives

$$\begin{aligned} \frac{\bar{q}_c z}{h_{fg}} = \frac{\rho_l}{\mu_l R} \left\{ \left[\frac{\partial p_v}{\partial z} - \rho_l (\omega^2 \bar{Z} - g \cos \theta) \sin \phi \right] \left(-\frac{1}{3} R \delta^3 + \frac{5}{24} \delta^4 \right) - \tau_{v,R-\delta} \left(\frac{1}{2} R \delta^2 - \frac{1}{3} \delta^3 \right) \right. \\ \left. - \rho_l \omega^2 \sin \phi \cos \phi \left(\frac{1}{8} R \delta^4 - \frac{3}{40} \delta^5 \right) \right\} \quad (2.45) \end{aligned}$$

Rearranging Eq. (2.45), the general solution for the liquid film thickness is

$$\begin{aligned} - \frac{3h_{fg}}{40\mu_l R \bar{q}_c z} \rho_l^2 \omega^2 \sin \phi \cos \phi \delta^5 + \frac{5h_{fg}\rho_l}{24\mu_l R \bar{q}_c z} [\rho_l (\omega^2 \bar{Z} - g \cos \theta) \sin \phi - \frac{\partial p_v}{\partial z}] \delta^4 - \frac{h_{fg}\rho_l}{3\mu_l R \bar{q}_c z} \delta^3 + \\ \frac{h_{fg}}{8\mu_l \bar{q}_c z} \rho_l^2 \omega^2 \sin \phi \cos \phi \delta^4 - \frac{h_{fg}\rho_l}{3\mu_l \bar{q}_c z} [\rho_l (\omega^2 \bar{Z} - g \cos \theta) \sin \phi - \frac{\partial p_v}{\partial z}] \delta^3 + \frac{h_{fg}\rho_l}{2\mu_l \bar{q}_c z} \tau_{v,R-\delta} \delta^2 + 1 = 0 \quad (2.46) \end{aligned}$$

If $\delta \ll R$, plugging $r \cong R$ into Eq. (2.43), it can be simplified as

$$\begin{aligned} \Gamma_l = \frac{m_l}{\pi D} \cong \int_{R-\delta}^R \rho_l w_l dr \\ = \frac{\rho_l}{\mu_l} \left\{ -\rho_l \omega^2 \sin \phi \cos \phi \frac{\delta^4}{8} - \left[\frac{\partial p_v}{\partial z} - \rho_l (\omega^2 \bar{Z} - g \cos \theta) \sin \phi \right] \frac{\delta^3}{3} - \tau_{v,R-\delta} \frac{\delta^2}{2} \right\} \quad (2.47) \end{aligned}$$

Substituting Eq.(2.44) into Eq. (2.47) and rearranging it, a simplified version of Eq.

(2.46) can be obtained

$$\frac{h_{fg}}{8\mu_l \bar{q}_c z} \rho_l^2 \omega^2 \sin \phi \cos \phi \delta^4 - \frac{h_{fg} \rho_l}{3\mu_l \bar{q}_c z} [\rho_l (\omega^2 \bar{Z} - g \cos \theta) \sin \phi - \frac{\partial p_v}{\partial z}] \delta^3 + \frac{h_{fg} \rho_l}{2\mu_l \bar{q}_c z} \tau_{v,R-\delta} \delta^2 + 1 = 0 \quad (2.48)$$

Eq. (2.48) is the same as the liquid film thickness over a plane geometry with a tilt angle (Cao and Chang, 1997), since the cylindrical surface can be treated as a plane surface if $R \gg \delta$. Therefore, Eq. (2.48) can also be used for the calculation of liquid film thickness for a plane geometry with a tilt angle.

If the tilt angle, ϕ , is 90° , then the equation for the liquid film thickness can be simplified further as

$$-\frac{h_{fg} \rho_l}{3\mu_l \bar{q}_c z} [\rho_l (\omega^2 \bar{Z} - g \cos \theta) \sin \phi - \frac{dp_v}{dz}] \delta^3 + \frac{h_{fg} \rho_l}{2\mu_l \bar{q}_c z} \tau_{v,R-\delta} \delta^2 + 1 = 0 \quad (2.49)$$

Eq. (2.49) and Eq. (2.20) are exactly the same because both of them are the equation of the liquid film thickness for a cylindrical heat pipe with $\phi = 90^\circ$.

Comparing Eq. (2.48) with Eq. (2.46), it is clear that Eq. (2.48) can be obtained from Eq. (2.46) if the first, second and third terms on the left-hand side of Eq. (2.46) are dropped. Also, Eq. (2.49) is obtained from Eq. (2.48) with $\phi = 90^\circ$. For these reasons, Eqs. (2.48), (2.20) and (2.49) are three special cases of Eq. (2.46). In other words, Eq. (2.46) is the general relation for liquid film distributions in radially rotating heat pipes.

After the liquid film thickness, δ , is obtained from the equations for the liquid film thickness, the temperature drop across liquid film thickness is

$$\Delta T_l = T_\delta - T_p = \frac{R \bar{q}_c \ln \frac{R}{R-\delta}}{k_l} \quad (2.50)$$

If the temperature distribution of liquid film is linear, the temperature drop across the liquid film can be expressed as

$$\Delta T_l = T_\delta - T_p = \frac{\bar{q}_c \delta}{k_l} \quad (2.51)$$

The local heat transfer coefficient, h_z , and local Nusselt number, Nu_z , in the condenser section can be the same as Eqs. (2.22) and (2.23), respectively.

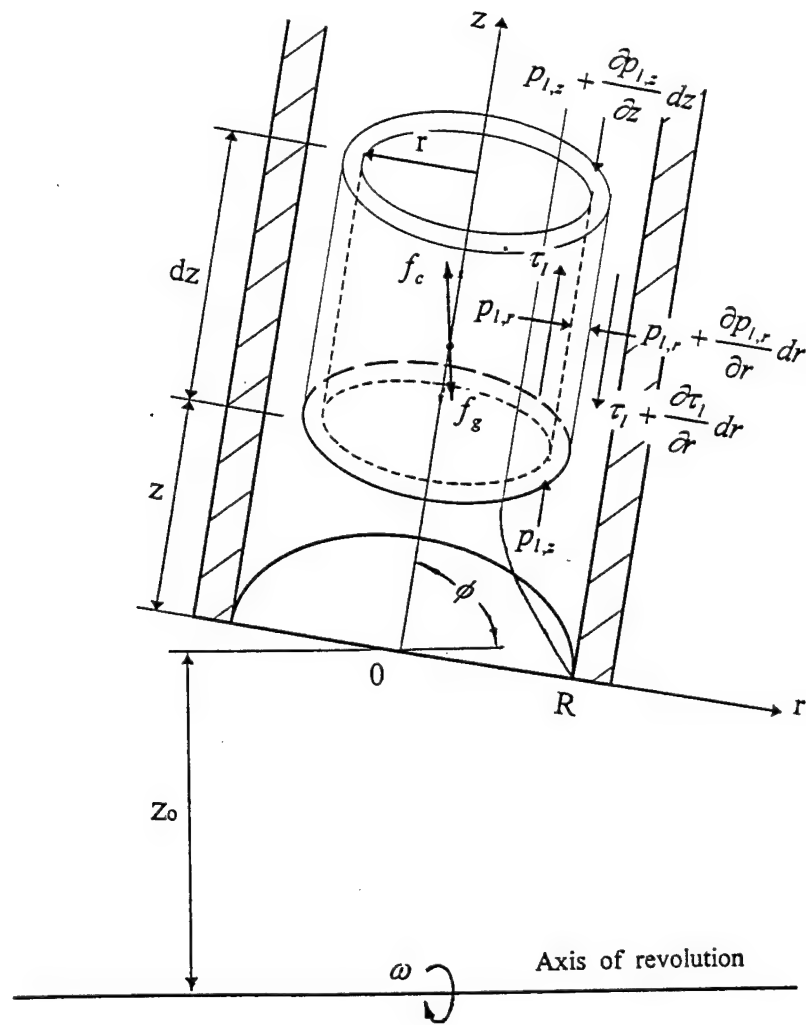


Fig. 2.4 Schematic of a differential control volume in the condensate film.

2.3 Axial Vapor Flow Analyses along the Heat Pipe Length

In the foregoing analytical solutions for the liquid film distributions on the heat pipe wall, both the shear stress at the liquid-vapor interface and the vapor pressure gradient along the heat pipe length are present. To complete the analysis, solutions for the vapor flow must be obtained. Also, as mentioned in the introduction, the centrifugal force may play an important role in the vapor temperature drop along the heat pipe length. In some extreme cases, this temperature drop may present a heat transfer limitation for the heat pipe performance. As a result, it is necessary to obtain the temperature drop along the heat pipe length. Consider a one-dimensional, laminar, and incompressible vapor flow along the heat pipe length under the steady-state operating condition, as shown in Fig. 2.5, where $f_c = \rho_v \omega^2 \bar{Z} \pi R_v^2 \sin \phi dz$ is the centrifugal force of the vapor, and $f_g = \rho_v g \pi R_v^2 \sin \phi \cos \theta dz$ is the gravitational force of the vapor. The momentum equation for the vapor flow is

$$\begin{aligned} p_v \pi R_v^2 \sin \phi - (p_v + \frac{dp_v}{dz} dz) \pi R_v^2 \sin \phi + \tau_{v,R_v} 2\pi R_v dz + \rho_v (\omega^2 \bar{Z} - g \cos \theta) \pi R_v^2 \sin \phi dz \\ = \dot{m}_v \bar{w}_v - [\dot{m}_v \bar{w}_v + \frac{d}{dz} (\dot{m}_v \bar{w}_v) dz] \end{aligned} \quad (2.52)$$

Eq. (2.52) can be simplified as

$$\frac{dp_v}{dz} = \frac{2}{R_v \sin \phi} \tau_{v,R_v} + \rho_v (\omega^2 \bar{Z} - g \cos \theta) - \frac{d}{dz} (\dot{m}_v \bar{w}_v) \frac{1}{\pi R_v^2 \sin \phi} \quad (2.53)$$

Since the shear stress of the vapor flow is

$$\tau_{v,R_v} = \frac{1}{2} f \rho_v \bar{w}_v^2 = f \left(\frac{2 \bar{w}_v R_v \rho_v}{\mu_v} \right) \left(\frac{\mu_v}{2 \bar{w}_v R_v \rho_v} \right) \frac{1}{2} \rho_v \bar{w}_v^2 = (f \text{Re})_v \frac{\mu_v \bar{w}_v}{4 R_v} \quad (2.54)$$

where $R_v = R - \delta$ is the vapor space radius in the heat pipe, \dot{m}_v is the vapor mass flow rate, \bar{w}_v is the average vapor velocity over the heat pipe cross-sectional area, and f is the laminar vapor skin-friction coefficient.

A thermal balance in the condenser section, as shown in Fig. 2.6, gives

$$\dot{m}_v = \frac{2 \pi R_v \bar{q}_c z}{h_{fg}} = \pi R_v^2 \rho_v \bar{w}_v \quad (2.55)$$

Therefore, $\bar{w}_v = \frac{2 \bar{q}_c z}{R_v \rho_v h_{fg}}$. Substituting it into Eq. (2.54) yields

$$\tau_{v,R_v} = (f \text{Re})_v \frac{\mu_v \bar{q}_c z}{2 R_v^2 \rho_v h_{fg}} \quad (2.56)$$

Since

$$\frac{d(m_v \bar{w}_v)}{dz} = 2 \pi R_v^2 \rho_v \bar{w}_v \frac{d \bar{w}_v}{dz} = \frac{8 \pi \bar{q}_c^2 z}{\rho_v h_{fg}^2} \quad (2.57)$$

Plugging Eqs. (2.56) and (2.57) into Eq. (2.53) gives

$$\frac{dp_v}{dz} = (f \text{Re})_v \frac{\mu_v \bar{q}_c z}{R_v^3 \rho_v h_{fg} \sin \phi} + \rho_l (\omega^2 \bar{Z} - g \cos \theta) - \frac{8 \bar{q}_c^2 z}{\rho_v R_v^2 h_{fg}^2 \sin \phi} \quad (2.58)$$

In general, the above equations are valid when the following two conditions in terms of the vapor Reynolds number and Mach number are satisfied:

$$\text{Re}_v = \frac{2 R_v Q}{A_v \mu_v h_{fg}} \leq 2300 \quad (2.59)$$

$$M_v = \frac{Q}{A_v \rho_v h_{fg} \sqrt{\gamma_v R_g T_v}} \leq 0.3 \quad (2.60)$$

where A_v is the cross-sectional area of the vapor space, γ_v is the vapor specific heat ratio, R_g is the gas constant of the vapor (Chi, 1976). These two conditions are usually satisfied for high-temperature heat pipes having a small diameter and operating at a steady state.

Assuming that the heat addition along the evaporator and the heat removal along the condenser are constant, the axial mass flow rate of vapor can be found by a mass and energy balance under the steady state (Faghri, 1995).

$$m_v = \frac{q_z}{h_{fg}} = \begin{cases} \frac{Q_c z}{L_c h_{fg}} & 0 \leq z \leq L_c \\ \frac{Q_c}{h_{fg}} & L_c \leq z \leq L_c + L_a \\ \frac{L - z}{L - (L_c + L_a)} \frac{Q_c}{h_{fg}} & L_c + L_a \leq z \leq L \end{cases} \quad (2.61)$$

where q_z is axial heat transfer rate of the vapor.

Substituting Eq. (2.61) into Eq. (2.55) and rearranging it

$$\frac{1}{q_c z} = \frac{m_v h_{fg}}{2\pi R_v} = \begin{cases} \frac{Q_c z}{2\pi R_v L_c} & 0 \leq z \leq L_c \\ \frac{Q_c}{L_c h_{fg}} \frac{h_{fg}}{2\pi R_v} & L_c \leq z \leq L_c + L_a \\ \frac{Q_c}{h_{fg}} \frac{h_{fg}}{2\pi R_v} \frac{L - z}{L - (L_c + L_a) h_{fg}} & L_c + L_a \leq z \leq L \end{cases} \quad (2.62)$$

Plugging Eq. (2.62) into Eq. (2.58) and integrating it from 0 to L , the vapor pressure drop along the heat pipe is

$$\Delta p_v = \int_0^L \frac{dp_v}{dz} dz = \frac{1}{\sin \phi} \int_0^L (f \text{Re})_v \frac{\mu_v \bar{q}_c z}{R_v^3 \rho_v h_{fg}} dz + \int_0^L \rho_v (\omega^2 \bar{Z} - g \cos \theta) dz - \frac{1}{\sin \phi} \int_0^L \frac{8 \bar{q}_c^2 z}{\rho_v R_v^2 h_{fg}^2} dz \quad (2.63)$$

Since the vapor momentum are very small, and can be negligible, the vapor pressure drop along heat pipe can be simplified as

$$\begin{aligned} \Delta p_v &= \frac{1}{\sin \phi} F_v Q_c \left(\frac{L_c + 2L_a + L_e}{2} \right) + \rho_v \omega^2 L \left(z_0 + \frac{L}{2} \sin \phi \right) - \rho_v L g \cos \theta \\ &= \frac{1}{\sin \phi} F_v L_{eff} Q_c + \rho_v \omega^2 L \bar{Z}_a - \rho_v L g \cos \theta \end{aligned} \quad (2.64)$$

where L is the heat pipe length, $L_{eff} = \frac{1}{2}(L_c + 2L_a + L_e)$ is the effective length of the heat pipe, $F_v = \frac{(f \text{Re})_v \mu_v}{2\pi R_v^4 \rho_v h_{fg}}$ is vapor frictional coefficient, $\bar{Z}_a = z_0 + \frac{1}{2} L \sin \phi$ is average revolving radius of the heat pipe, and $Q_c = Q_e = \pi D L_c \bar{q}_c$ is the total heat transfer rate at the condenser or evaporator section at a steady state.

As mentioned earlier, the vapor Reynolds number is in general less than 2300. But with an increase in the total heat input Q , the Mach number may be greater than 0.3 when the heat pipe operating temperature is relatively low. In this situation, the vapor compressibility should be taken into consideration. Based upon the bulk fluid properties, the ratio of the drag coefficient for a compressible flow, $f_{v,c}$, to that for an incompressible flow, $f_{v,i}$, at the same vapor Reynolds number can be corrected by the following equation (Chi, 1976):

$$\frac{f_{v,c}}{f_{v,i}} = \left(1 + \frac{\gamma_v - 1}{2} M_v^2\right)^{-\frac{1}{2}} \quad (2.65)$$

Substituting Eq. (2.65) into the relation for the vapor frictional coefficient, a modified vapor friction coefficient is obtained:

$$F_v = \frac{(f \text{Re}_v) \mu_v}{2\pi R_v^4 \rho_v h_{fg}} \left(1 + \frac{\gamma_v + 1}{2} M_v^2\right)^{-\frac{1}{2}} \quad (2.66)$$

In fact, the vapor pressure drop caused by the gravity is very small, and can be negligible. Therefore, the vapor pressure drop along the heat pipe length becomes

$$\Delta p_v = \frac{F_v L_{eff}}{\sin \phi} Q_c + \rho_v \omega^2 L \bar{Z}_a \quad (2.67)$$

The Clapeyron equation that relates the saturated temperature to the saturated pressure is

$$\Delta p_v = \frac{h_{fg} \rho_v}{T_v} \Delta T_v \quad (2.68)$$

Substituting Eq. (2.68) into Eq. (2.67), the vapor temperature drop along the heat pipe length is

$$\Delta T_v = \frac{T_v}{h_{fg} \rho_v} \Delta p_v = \frac{T_v L_{eff} F_v}{\rho_v h_{fg} \sin \phi} Q_c + \frac{T_v}{h_{fg}} \omega^2 L \bar{Z}_a = \Delta T_{v,f} + \Delta T_{v,c} \quad (2.69)$$

The dimensionless temperature drop of the vapor along the heat pipe length is

$$\frac{\Delta T_v}{T_v} = \frac{L_{eff} F_v}{\rho_v h_{fg} \sin \phi} Q_c + \frac{\omega^2 L \bar{Z}_a}{h_{fg}} = \frac{\Delta T_{v,f}}{T_v} + \frac{\Delta T_{v,c}}{T_v} = \Delta T_f + \Delta T_c \quad (2.70)$$

where ΔT_v is the total vapor temperature drop along the heat pipe length, T_v is the operating temperature of the heat pipe, ΔT_f is the dimensionless temperature drop due to friction at the liquid-vapor interface, and ΔT_c is the dimensionless temperature drop due to the vapor centrifugal force.

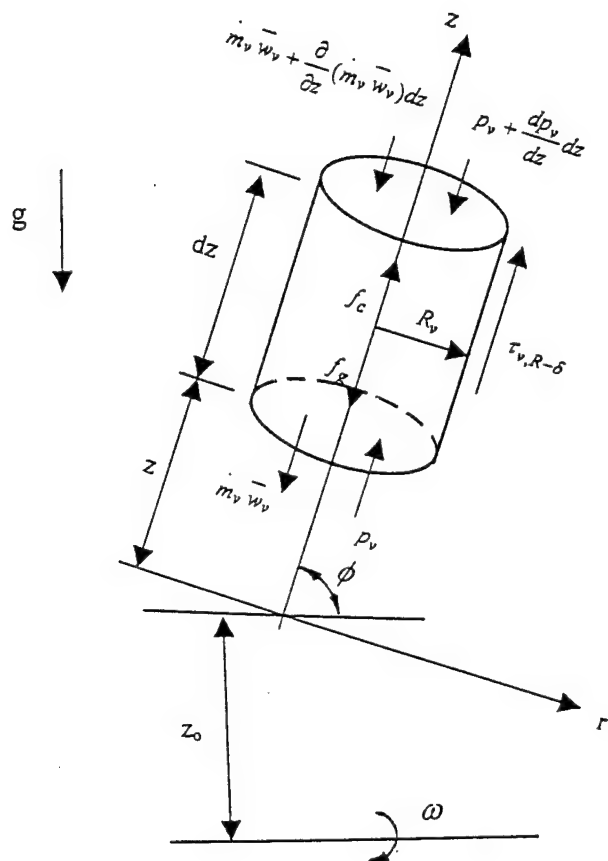


Fig. 2.5 Schematic of a vapor thermal balance in the condenser section.

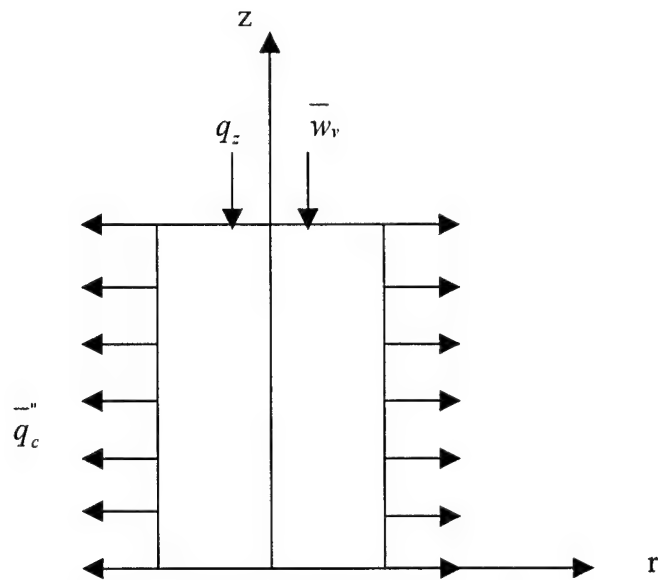


Fig. 2.6 Schematic of an overall thermal balance in the condenser section.

2.4 Analytical Results for the Temperature Drops and Heat Transfer Limitations

Temperature drops across the liquid film or along the heat pipe length are very important criteria for designing radially rotating miniature heat pipes with a high operating temperature and rotating speed. In order to prove the feasibility of the turbine blade cooling application, analytical results are presented for radially rotating miniature heat pipes working under high heat flux and high rotating speed conditions. The ranges of heat inputs, geometric dimensions, and the rotating speeds are as follows: $40 \text{ W} \leq Q \leq 200 \text{ W}$, $1 \text{ mm} \leq d_i \leq 8 \text{ mm}$, $6.26 \leq \omega^2 \bar{Z}_a / g \leq 6.26 \times 10^5$, $L = 80 \text{ mm}$, $L_c = L_e = 40 \text{ mm}$, $L_a = 0$, and $\phi = 90^\circ$. It should be pointed out that these ranges are only close to the turbine blade cooling conditions, not real design values (Harman, 1981). It is clear that, according to Eqs. (2.46) through (2.70), the liquid film thickness, temperature drop across the liquid film, and vapor temperature drop along the heat pipe length are mainly the function of shear stresses, heat fluxes, liquid and vapor thermophysical properties, liquid and vapor centrifugal forces, heat pipe sizes, and heat pipe operating temperatures. The operation of a heat pipe depends on the heat load in the evaporator and the cooling condition in the condenser. In general, the operating temperature, T_v , of a heat pipe can be controlled by the flow rate of cooling air in the condenser section and heat input in the evaporator section. The operating temperature, T_v , will be going up if the flow rate of the cooling air is reduced or the heat input is increased.

Fig. 2.7 illustrates the maximum temperature drops across the liquid film versus the dimensionless centrifugal forces, $\omega^2 \bar{Z}_a / g$, for sodium as the working fluid. The

working temperature, T_v , and the total heat input, Q , are kept as constants at 1100 K and 200 W, respectively. The dimensionless geometric parameter, d_i/L , is treated as a variable. For the results presented in Fig. 2.8, however, d_i/L is kept as a constant, and the operating temperature is considered to be a variable. It is observed from Figs. 2.7 and 2.8 that at a relatively high rotating speed or large revolving radius, $\omega^2 \bar{Z}_a / g > 150$, the maximum temperature drop across the liquid film is negligible. However, a small heat pipe diameter or a low heat pipe operating temperature may increase the temperature drop. Still, under normal turbine working conditions, the maximum temperature drop is much less than 1 K. This means that the commonly encountered condenser limitation for low-temperature heat pipes would never be a serious problem for the high-temperature heat pipes studied in this report.

Calculations are then made for the vapor temperature drops along the heat pipe length with sodium and potassium as the working fluids. Fig. 2.9 shows vapor temperature drops as a function of dimensionless centrifugal forces at different operating temperatures. The dimensionless heat pipe geometric parameter and the total heat input are kept as constants ($d_i/L = 0.025$ and $Q = 200$ W). It is clear from the figure that the vapor temperature drops increase with an increase in the centrifugal force or in the operating temperature. At the same time, it can be seen that a heat pipe with sodium as the working fluid would have a smaller vapor temperature drop than the heat pipe with potassium as the working fluid. For many cases, the vapor temperature drop is on the order of 10-40 K. This temperature drop is considerably high for a low-temperature heat pipe. However, for the high-temperature heat pipes studied in this report, this temperature

drop is relatively small compared to the average heat pipe operating temperature level.

The vapor temperature drops as a function of heat pipe operating temperatures and dimensionless size are shown in Fig. 2.10. At a given heat pipe operating temperature, the vapor temperature drop is increased when the heat pipe diameter is decreased due to a higher friction at the liquid-vapor interface. If the heat pipe operating temperature is less than 1100 K, the vapor temperature drops for the miniature heat pipe with $d_i/L=0.0125$ would increase sharply. However, for a heat pipe with a d_i/L greater than 0.02 or d_i greater than 1.5 mm, the influence of the operating temperature level on the vapor temperature drop is relatively small.

Fig. 2.11 illustrates the influence of the heat input on the vapor temperature drop along the heat pipe length. In general, the influence of the heat input on the vapor temperature drop is relatively small when the operating temperature level of the heat pipe is relatively high. However, for a heat pipe operating at a relatively low temperature level, the vapor temperature drop is substantially increased when the heat input is high.

According to Eq. (2.70), the total vapor temperature drop is due to the contributions of friction at the liquid-vapor interface and the vapor centrifugal force in the heat pipe. The contribution of the centrifugal force is illustrated in Fig. 2.12 as the ratio of the vapor temperature drop due to the vapor centrifugal force to the total vapor temperature drop. At a low rotating speed, the contribution of the centrifugal force is relatively small, but at a high rotating speed, the contribution of the centrifugal force becomes a dominant factor. This is especially obvious for a heat pipe having a relatively large diameter.

As illustrated by the foregoing analytical results, the vapor temperature drop along the heat pipe length may present a heat transfer limitation when the heat pipe is of very small diameter, with a relatively low operating temperature level and high rotating speed. However, for a miniature heat pipe having a diameter on the order of 1.5 to 2 mm, the heat transfer limitation would not be encountered at normal rotating speeds and operating temperature levels. This indicates that the radially rotating miniature heat pipe is feasible for the turbine blade cooling application.

The entrainment limit is due to the interaction between the countercurrent liquid and vapor flows occurring at the liquid-vapor interface. This limit may be a major concern when the heat input is high and the heat pipe dimensionless sizes are small. In this case, the shear stresses at the liquid-vapor interface retard the return of the liquid from the condenser to the evaporator section. The heat pipe is said to have reached the entrainment limit when the liquid is prohibited from returning to the evaporator section. A comprehensive review regarding the entrainment limit for two-phase closed thermosyphons is given by Faghri (1995) and Peterson (1994). Various correlations for the evaluation of this limit are also included in the literature. For current wickless rotating heat pipes, the mechanism of the entrainment limit should be similar to that of thermosyphons with the gravitational force being replaced by the rotating centrifugal force. Fig. 2.13 shows the entrainment limits for the same heat pipe studied earlier at different rotating speeds. The calculation was made based on Wallis' correlation (Faghri, 1995)

$$\frac{Q_{ent}}{A} = \frac{C_w^2 h_{fg} \sqrt{(r_0 + z) \omega^2 D (\rho_l - \rho_v) \rho_v}}{[1 + (\rho_v / \rho_l)^{1/4}]^2} \quad (2.71)$$

and the correlation from Faghri et al. (1989)

$$\frac{Q_{ent}}{A} = (\rho_l / \rho_v)^{0.14} (\tanh^2 Bo^{\frac{1}{4}}) h_{fg} [(r_0 + z) \omega^2 \sigma (\rho_l - \rho_v)]^{1/4} [\rho_l^{-1/4} + \rho_v^{-1/4}]^{-2} \quad (2.72)$$

for sodium and potassium as the working fluids. For the rotating heat pipe with a small dimensionless size, $d_i / L = 0.0125$, the entrainment limit is very sensitive to the rotating speed, and it may be a concern when the rotating speed is very low. However, when the rotating speed is moderately high, the entrainment limit is increased to more than 100 W/cm², which is acceptable for turbomachinery applications. The values of the entrainment limit that are calculated by the Wallis' correlation are close to those from Faghri et al. (1989), when the rotating speed is low. However, at high rotating speeds, large deviation occurs with both working fluids. A similar trend was observed also by Faghri (1995) for thermosyphons.

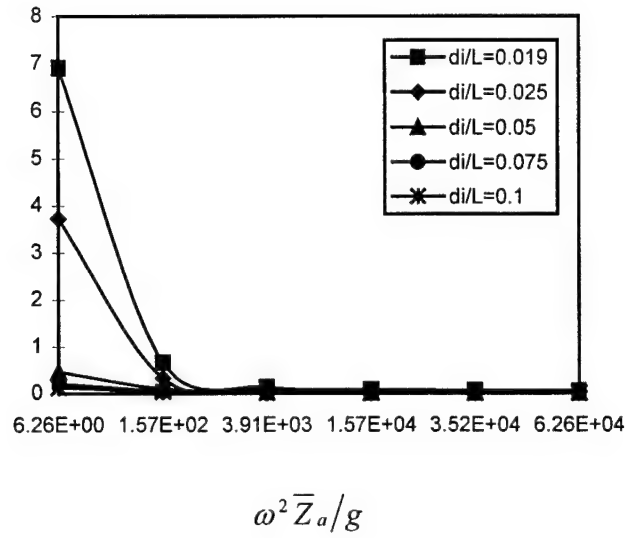


Fig. 2.7 Maximum temperature drops across the liquid film for sodium as the working fluid ($T_v = 1100$ K, $Q = 200$ W).

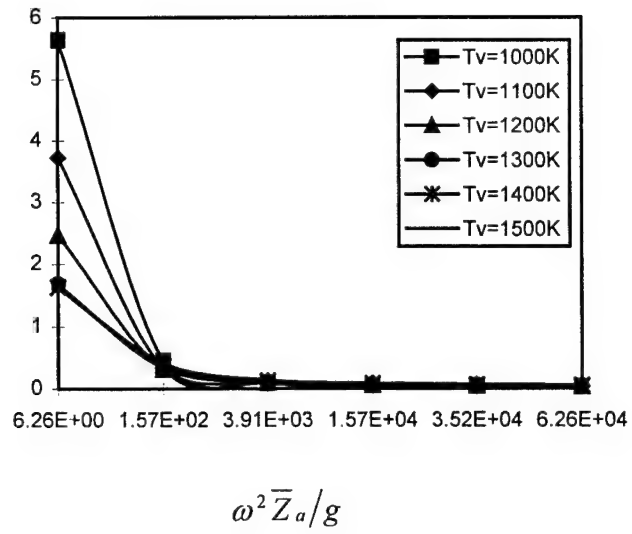
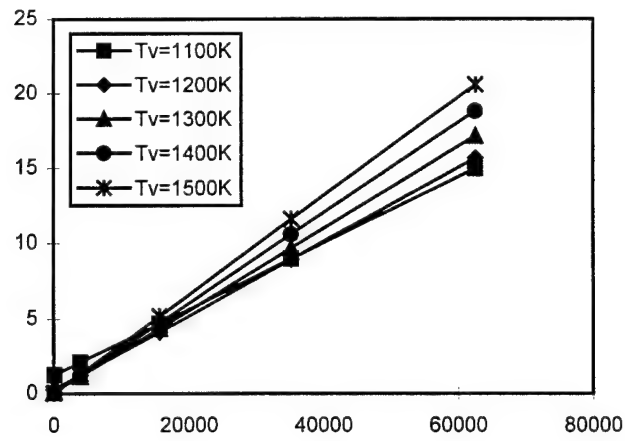
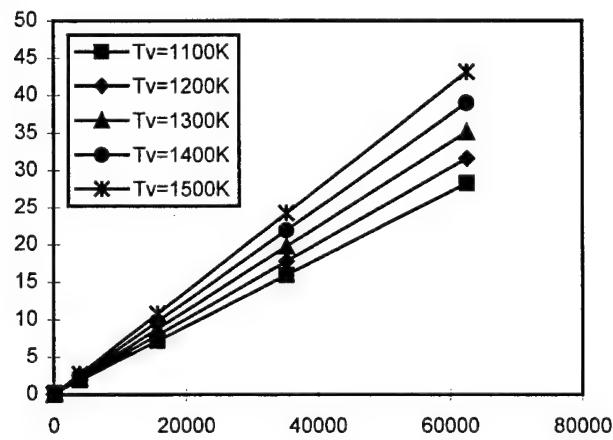


Fig. 2.8 Maximum temperature drops across the liquid film for sodium as the working fluid ($d_i/L = 0.025$, $Q = 200$ W).



(a) Sodium



(b) Potassium

Fig. 2.9 Vapor temperature drops along the heat pipe length at different rotating speeds ($d_i / L = 0.025$, $Q = 200$ W).

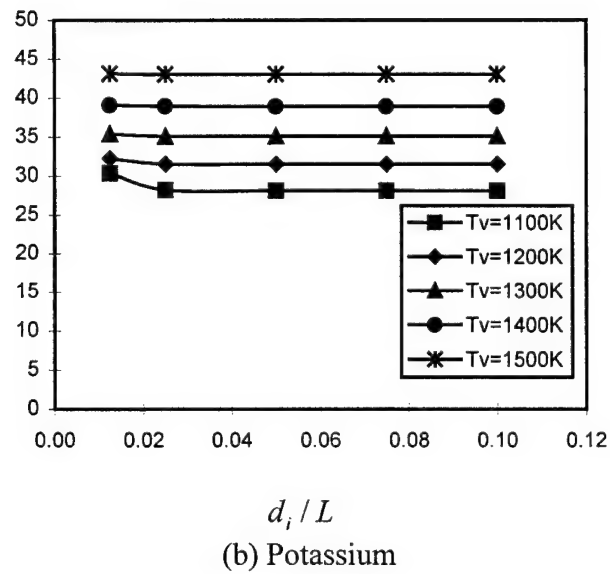
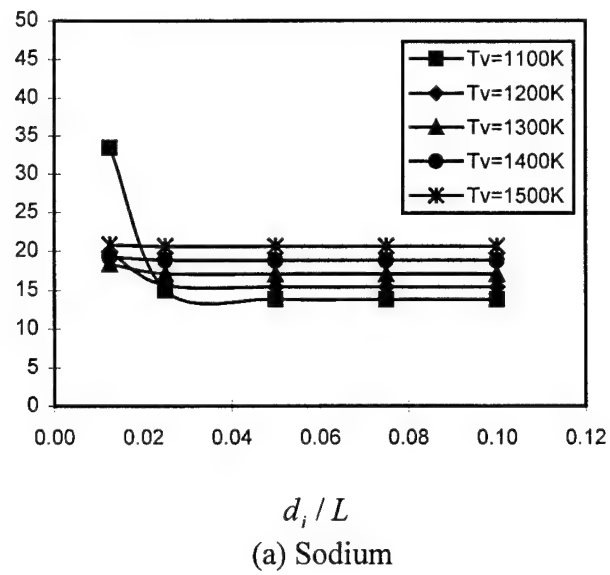
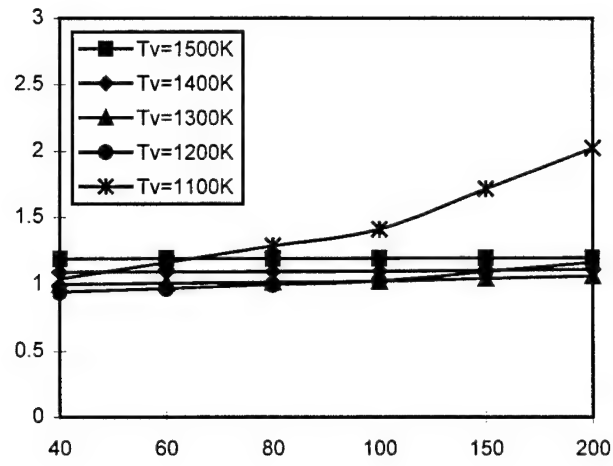
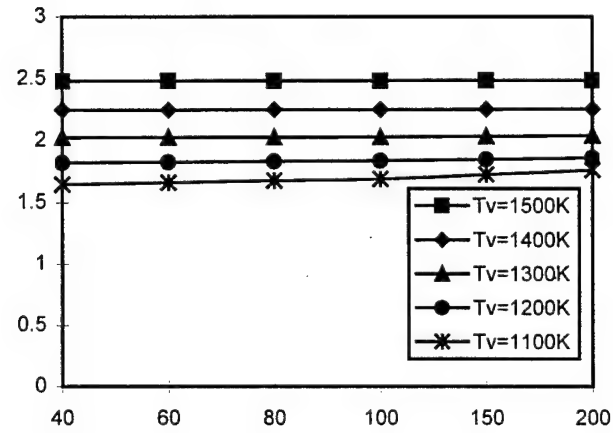


Fig. 2.10 Vapor temperature drops along the heat pipe length at different heat pipe dimensionless sizes ($Q=200$ W, $\omega^2 \bar{Z}_a / g = 6.26 \times 10^4$).



Q (W)
(a) Sodium



Q (W)
(b) Potassium

Fig. 2.11 Vapor temperature drops along the heat pipe length at different heat inputs ($d_i / L = 0.025$, $\omega^2 \bar{Z}_a / g = 3.91 \times 10^3$).

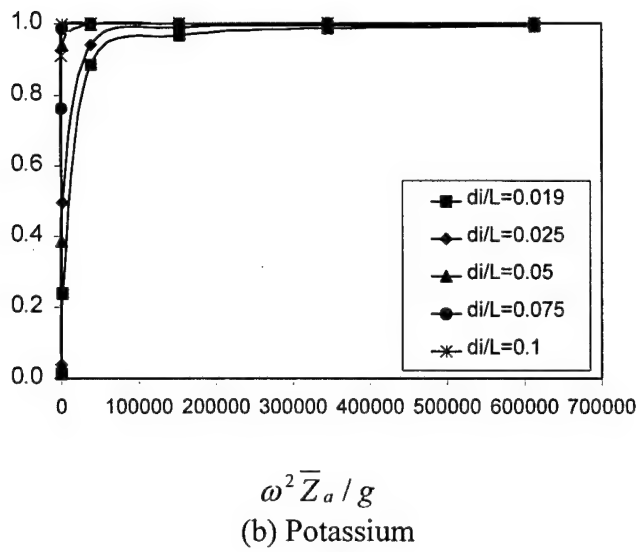
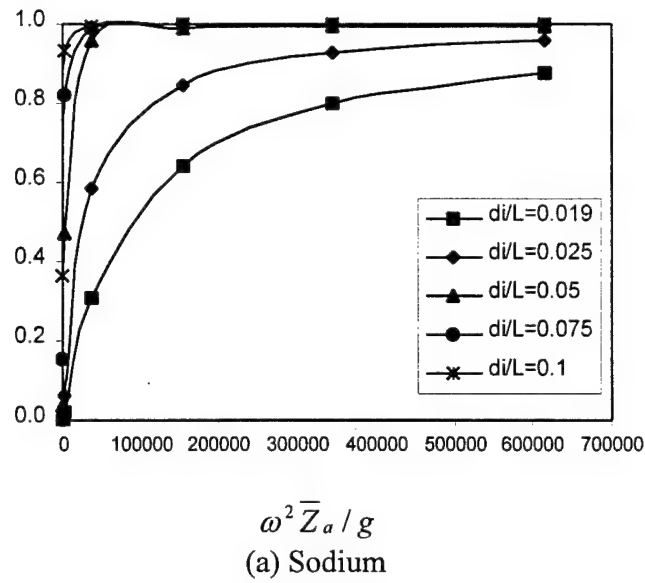


Fig. 2.12 Ratio of the vapor temperature drops due to the centrifugal force to the total temperature drop ($T_v=1100$ K, $Q=200$ W).

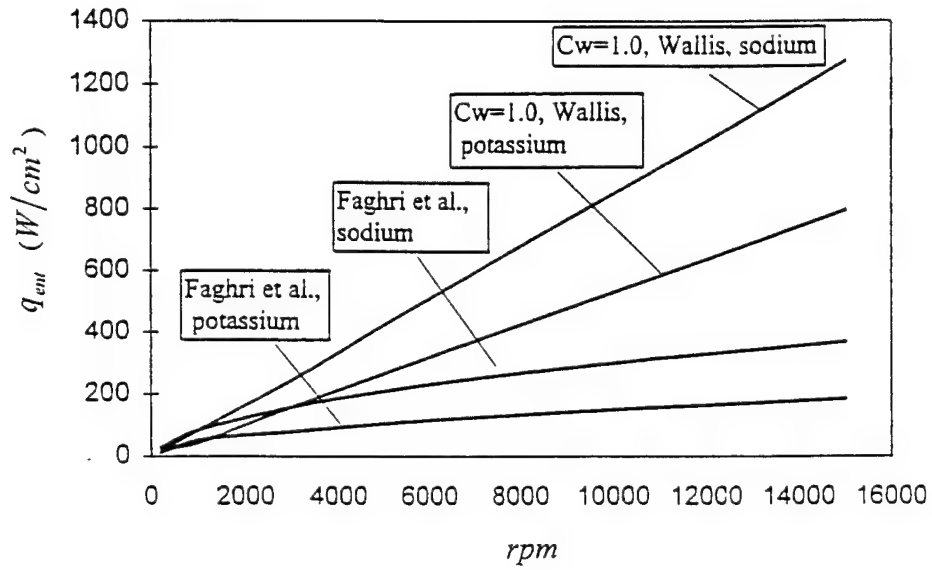


Fig. 2.13 Entrainment limitations as a function of rotating speeds ($T_{ref}=937$ K for potassium and $T_{ref}=1073$ K for sodium).

3. TEMPERATURE DISTRIBUTIONS ALONG THE HEAT PIPE AND DIFFUSE EFFECTS OF NON-CONDENSABLE GASES

3.1 Analysis of Vapor Temperature Distribution along the Heat Pipe

Temperature distributions along the heat pipe length play an important role in the heat transfer efficiency of the heat pipe. Vapor temperature drop for traditional heat pipes without rotation are mainly due to the vapor friction. The vapor temperature is almost uniform since the vapor friction is generally small. But for radially rotating heat pipes, the temperature drop is caused not only by the vapor friction but also by the centrifugal force. Therefore, the temperature drop for a radially rotating heat pipe is larger than that for a traditional heat pipe.

For the vapor momentum equation in chapter 2.3, the last term of the right-side in Eq. (2.53) is usually negligible compared to the other terms, and the pressure gradient Eq. (2.53) becomes

$$\frac{dp_v}{dz} = (f \text{ Re})_v \frac{\mu_l \bar{q}_c z}{R_v^3 \rho_v h_{fg} \sin \phi} + \rho_l (\omega^2 \bar{Z} - g \cos \theta) \quad (3.1)$$

In addition, for the practical application of blade cooling, the adiabatic length, L_a , is zero. Therefore, the heat pipe is divided only into the evaporator and condenser sections. Integrating Eq. (3.1) from 0 to z based on the mass and energy balance under the steady state in Eq. (2.62) and $L_a = 0$ yields,

$$\begin{aligned}
\Delta p_{v,z} &= \int_0^z \frac{dp_v}{dz} dz \\
&= \frac{1}{\sin \phi} (f \text{Re})_v \frac{\mu_v Q_c}{2\pi R_v^4 \rho_v h_{fg}} \int_0^z \frac{z}{L_c} dz + \rho_v \int_0^z [\omega^2 (z_0 + z \sin \phi) - g \cos \theta] dz \\
&= \frac{F_v Q_c z^2}{2L_c \sin \phi} + \rho_v [\omega^2 (z_0 + \frac{1}{2} z \sin \phi) z - g \cos \theta] \quad \text{for } 0 \leq z \leq L_c \quad (3.2)
\end{aligned}$$

$$\begin{aligned}
\Delta p_{v,z} &= \int_0^z \frac{dp_v}{dz} dz \\
&= \frac{1}{\sin \phi} (f \text{Re})_v \frac{\mu_v Q_c}{2\pi R_v^4 \rho_v h_{fg}} \left[\int_0^{L_c} z dz + \int_{L_c}^z \frac{L-z}{L-L_c} dz \right] + \rho_v \int_0^z [\omega^2 (z_0 + z \sin \phi) - g \cos \theta] dz \\
&= \frac{F_v Q_c}{2 \sin \phi} \left[L - \frac{(L-z)^2}{L-L_c} \right] + \rho_v [\omega^2 (z_0 + \frac{1}{2} z \sin \phi) z - g \cos \theta] \quad \text{for } L_c \leq z \leq L \quad (3.3)
\end{aligned}$$

The vapor gravitational force can be neglected compared to the centrifugal force in Eqs.(3.2) and (3.3). According to Clapeyron Equation, we have

$$\Delta T_{v,z} = \begin{cases} \frac{T_v F_v Q_c}{2h_{fg} \rho_v L_c \sin \phi} z^2 + \frac{T_v}{h_{fg}} [\omega^2 (z_0 + \frac{1}{2} z \sin \phi) z] & (0 \leq z \leq L_c) \\ \frac{T_v F_v Q_c}{2h_{fg} \rho_v \sin \phi} \left[L - \frac{(L-z)^2}{L-L_c} \right] + \frac{T_v}{h_{fg}} [\omega^2 (z_0 + \frac{1}{2} z \sin \phi) z] & (L_c \leq z \leq L) \end{cases} \quad (3.4)$$

since

$$\Delta T_{v,z} = T_{v,z} - T_{v,z_0} \quad (3.5)$$

$$T_{v,z_0} = T_{v,L} - \Delta T_v = T_{v,L} - \left[\frac{T_v F_v Q_c L_{eff}}{h_{fg} \rho_v \sin \phi} + \frac{T_v}{h_{fg}} \omega^2 (z_0 + \frac{1}{2} L \sin \phi) L \right] \quad (3.6)$$

substituting Eqs. (3.4) and (3.6) into (3.5) and rearranging it yield

$$\begin{aligned}
T_{v,z} &= T_{v,z_0} + \Delta T_{v,z} = \\
T_{v,L} &- \begin{cases} \left\{ \frac{T_v F_v Q_c}{h_{fg} \rho_v \sin \phi} (L_{eff} - \frac{z^2}{2L_c}) + \frac{T_v \sin \phi}{h_{fg}} \omega^2 [(z_0 + \frac{1}{2}L)L - (z_0 + \frac{1}{2}z)z] \right\} & 0 \leq z \leq L_c \\ \left\{ \frac{T_v F_v Q_c}{h_{fg} \rho_v \sin \phi} [L_{eff} - \frac{1}{2}(L - \frac{(L-z)^2}{L-L_c})] + \frac{T_v \sin \phi}{h_{fg}} \omega^2 [(z_0 + \frac{1}{2}L)L - (z_0 + \frac{1}{2}z)z] \right\} & L_c \leq z \leq L \end{cases}
\end{aligned} \tag{3.7}$$

where ΔT_v is the total vapor temperature drop along the heat pipe length, T_{v,z_0} and $T_{v,L}$ are the temperatures at the condenser and evaporator ends, respectively.

Eq. (3.7) gives an analytical solution for the temperature distributions along the heat pipe length. It should be pointed out that Eq. (3.7) only considers the effects of vapor friction and centrifugal force on the temperature distribution. If there are some non-condensable gases in the heat pipe, the diffuse effects of non-condensable gases on the temperature distribution must be included.

3.2 Analytical Solution of Temperature Distribution along the Heat Pipe Length Including the Diffuse Effects of Non-Condensable Gases

Because of the wickless structure and a very small volume of the radially rotating miniature heat pipes, it is possible to have a small amount of non-condensable gases remaining in the heat pipe during the procedure of charging and sealing. Non-condensable gases will be driven to the condenser end by the vapor from the evaporator, which prevent the vapor to fill the entire condenser section. Therefore, the temperature distribution along the condenser wall will not be uniform any more, and a large temperature drop will appear in the condenser section as a result of the existence of non-condensable gases. Marcus (1971) first developed a numerical model based on one-dimensional diffusion of the vapor-gas system coupled with one-dimensional axial heat conduction in the wall for variable conductance heat pipes. Numerical results indicated that the axial heat conduction plays a dominant role in the determination of the temperature distribution along the heat pipe wall.

For a radially rotating heat pipe, the vapor-gas interface between the vapor and non-condensable gases is assumed to be a flat front. Fig. 3.1 shows schematically a thermal balance for the heat pipe wall in the condenser section. A control volume of the cross-sectional area, $\pi(r_0^2 - r_i^2)$, and infinitesimal length, dz , is considered. Based on the conservation of energy,

$$\pi(r_0^2 - r_i^2)k_p \frac{dT}{dz} + 2\pi r_0 h_c (T_p - T_s)dz = \pi(r_0^2 - r_i^2)k_p \left(\frac{dT}{dz} + \frac{d^2T}{dz^2} dz \right) + Q' dz \quad (3.8)$$

Eq. (3.8) can be simplified as

$$\pi(r_0^2 - r_i^2)k_p \frac{d^2T}{dz^2} - 2\pi r_0 h_c (T_p - T_s) + Q' = 0 \quad (3.9)$$

Since the radial temperature drop in the heat pipe wall is much less than the axial temperature drop, the radial temperature drop can be neglected, that is, the temperature in the radial direction of heat pipe wall is uniform, $T_p = T$. Eq. (3.9) can be rearranged as

$$\frac{d^2T}{dz^2} - m^2 (T - T_s - \frac{Q'}{2\pi r_0 h_c}) = 0 \quad (3.10)$$

where

$$m^2 = \frac{2r_0 h_c}{k_p (r_0^2 - r_i^2)} \quad (3.11)$$

h_c is the mean heat transfer coefficient, Q' is the heat output in the condenser section without non-condensable gases, m is a coefficient, T is the axial temperature which is a function of z , T_p and T_s are the outer surface temperature of the heat pipe and surrounding temperature, respectively.

Assuming the distribution of Q' is uniform in the portion of the condenser section without non-condensable gases, and zero in the portion of the condenser section with non-condensable gases,

$$Q' = 0 \quad \text{for } 0 \leq z \leq L_{c,n} \quad (3.12)$$

$$Q' = \frac{Q_c}{L_c - L_{c,n}} \quad \text{for } L_{c,n} \leq z \leq L_c \quad (3.13)$$

where Q_c is total heat output in the condenser section; L_c is the lengths of the total condenser section and $L_{c,n}$ is the portion with the non-condensable gases, respectively.

At the inlet of the condenser section, the axial heat conduction is negligible,

$$Q_c \cong 2\pi r_0 (L_c - L_{c,n}) h_c (T_{L_c} - T_s) \quad (3.14)$$

where T_{L_c} is the temperature at the condenser inlet.

Substituting Eq. (3.14) into (3.13) and recasting it

$$\frac{Q_c}{2\pi r_0 h_c} = T_{L_c} - T_s \quad \text{at } L_{c,n} \leq z \leq L_c \quad (3.15)$$

plugging Eqs. (3.15) and (3.12) into (3.10) yields

$$\frac{d^2 T}{dz^2} - m^2 (T - T_s) = 0 \quad \text{at } 0 \leq z \leq L_{c,n} \quad (3.16)$$

$$\frac{d^2 T}{dz^2} - m^2 (T - T_{L_c}) = 0 \quad \text{at } L_{c,n} \leq z \leq L_c \quad (3.17)$$

For a radially rotating miniature heat pipe, the boundary conditions are

$$\frac{dT}{dz} = 0 \quad \text{at } z = -\infty \quad (3.18)$$

$$T = T_{L_c} \quad \text{at } z = L_c \quad (3.19)$$

According to the balance of total thermal energy in the condenser section,

$$\int_0^{L_c} 2\pi r_0 h_c (T - T_c) dz = Q_c \quad (3.20)$$

Solving Eqs. (3.16) and (3.17) yields

$$T = a \exp(mz) + b \exp(-mz) + T_s \quad \text{at } 0 \leq z \leq L_{c,n} \quad (3.21)$$

$$T = c \exp(mz) + d \exp(-mz) + T_{L_c} \quad \text{at } L_{c,n} \leq z \leq L_c \quad (3.22)$$

Applying boundary conditions Eqs. (3.18) and (3.19) to determine the constants in Eqs.

(3.21) and (3.22) gives

$$b = 0, \quad \text{and} \quad d = -c \exp(2mL_c)$$

Substituting coefficients, b and d , into Eqs. (3.21) and (3.22) results in

$$T = a \exp(mz) + T_s \quad \text{at } 0 \leq z \leq L_{c,n} \quad (3.23)$$

$$T = c \{ \exp(mz) - \exp[m(2L_c - z)] \} + T_{L_c} \quad \text{at } L_{c,n} \leq z \leq L_c \quad (3.24)$$

Because of the continuity of axial temperature distribution along the heat pipe length, the temperature in Eqs. (3.23) and (3.24) must be equal at $z = L_{c,n}$,

$$a \exp(mL_{c,n}) + T_s = c \{ \exp(mL_{c,n}) - \exp[m(2L_c - L_{c,n})] \} + T_{L_c} \quad (3.25)$$

Therefore,

$$c = \frac{a \exp(mL_{c,n}) - (T_{L_c} - T_s)}{\exp(mL_{c,n}) - \exp[m(2L_c - L_{c,n})]} \quad (3.26)$$

Substituting Eqs. (3.23) and (3.24) into (3.20) and rearranging it give

$$a \int_0^{L_c} \exp(mz) dz + \int_{L_{c,n}}^{L_c} \{ (T_{L_c} - T_s) + c [\exp(mz) - \exp(m(2L_c - z))] \} dz = \frac{Q_c}{2\pi r_0 h_c} \quad (3.27)$$

Plugging Eqs. (3.14) and (3.26) into Eq. (3.27), integrating and recasting it yield

$$a = \frac{(T_{L_c} - T_s) \{ 2 \exp(mL_c) - \exp(mL_{c,n}) - \exp[m(2L_c - L_{c,n})] \}}{2 \exp[m(L_c + L_{c,n})] + \exp[m(2L_c - L_{c,n})] - 2 \exp(2mL_c) - \exp(mL_{c,n})} \quad (3.28)$$

Substituting the coefficients, a and c , into Eqs. (3.23) and (3.24) gives the temperature distribution along the condenser section under the diffuse effects of non-condensable gases.

If $L_{c,n} = 0$, there is no non-condensable gas in the condenser section. Substituting

$L_{c,n} = 0$ into Eqs. (3.28) and (3.26), we get

$$a = T_{L_c} - T_s \quad \text{and} \quad c = 0$$

Plugging $a = T_{L_c} - T_s$ and $c = 0$ in Eqs. (3.23) and (3.24) yields

$$T = T_{L_c} \quad 0 \leq z \leq L$$

The above relation means that the temperature distribution along the condenser section is uniform under the condition of no temperature drops caused by the friction and centrifugal force. At the same time, it also proves the conclusion in chapter 2, in which the temperature drops along the heat pipe are mainly caused by the friction and centrifugal force if there are no non-condensable gases existing in the heat pipe.

It should be pointed out that since the radial temperature drop in the heat pipe wall is much smaller than the axial one and is neglected in the governing equation (3.10), the temperature in the heat pipe wall can represent the vapor temperature in this region proximately.

Substituting $z=0$ into Eq. (3.23), we can obtain the temperature at the end of the condenser section with diffuse effects of non-condensable gases,

$$T'_{z_0} = T_s + a \quad \text{at } z = 0 \quad (3.29)$$

Therefore, the temperature drops along the condenser section with the diffuse effects of non-condensable gases are

$$\Delta T_{n,z} = T - T'_{z_0} = \begin{cases} a[\exp(mz) - 1] & 0 \leq z \leq L_{c,n} \\ T_{L_c} - \{T_s + a + c[\exp(m(2L_c - z)) - \exp(mz)]\} & L_{c,n} \leq z \leq L_c \end{cases} \quad (3.30)$$

Usually, the amount of non-condensable gases in the condenser section is so small that their diffuse effects can not reach the evaporator section. Accordingly, the temperature distribution in the evaporator section is not affected by the diffuse of non-condensable gases, and Eq. (3.7) is still suitable for the temperature distribution along the evaporator section. But the temperature distribution in the condenser section will be affected strongly by the diffusion effects of non-condensable gases. At the same time, the

vapor temperature drop, $\Delta T_{v,z}$, caused by the friction and centrifugal force must be included in the temperature drop in the condenser section. If the temperature drop caused by the diffuse effects of non-condensable gases is superposed on the temperature drop produced by vapor friction and centrifugal force, the following relations are obtained

$$\Delta T_z = \Delta T_{v,z} + \Delta T_{n,z} \quad (3.31a)$$

$$\Delta T_{n,L_c} = T_{L_c} - T'_{z_0} = T_{L_c} - T_s - a \quad (3.31b)$$

$$T_{z_0} = T_{v,L} - \Delta T_v - \Delta T_{n,L_c} \quad (3.31c)$$

$$\Delta T_z = T_{v,z} - T_{z_0} \quad (3.31d)$$

where T_{z_0} is the temperature at the end of the condenser section with the diffuse effects of non-condensable gases and effects of the friction and centrifugal force in the heat pipe. Substituting Eqs. (3.31a), (3.31b), and (3.31c) into (3.31d) and rearranging it yield

$$T_{v,z} = T_{v,L} - T_{L_c} + T'_{z_0} - \Delta T_v + \Delta T_{v,z} + \Delta T_{n,z} \quad (3.32)$$

It should be pointed out that the temperature drop caused by the vapor friction and centrifugal force must be dropped from Eq. (3.32) in $0 \leq z \leq L_{c,n}$ since the vapor does not exist in this section. As a result, after the vapor temperature drops caused by vapor friction, centrifugal force, and diffuse effects of non-condensable gases are considered completely, the vapor temperature distributions along the heat pipe length are:

In the evaporator section,

$$T_{v,z} = T_{v,L} - \frac{T_v F_v Q_c}{h_{fg} \rho_v \sin \phi} \left\{ L_{eff} - \left[L - \frac{(L-z)^2}{L-L_c} \right] \right\} - \frac{T_v \omega^2 \sin \phi}{h_{fg}} \left[\left(z_0 + \frac{1}{2} L \right) L - \left(z_0 + \frac{1}{2} z \right) z \right] \quad (3.33)$$

$$L_c \leq z \leq L$$

In the condenser section,

$$T_{v,z} = T_{v,L} - T_{L_c} + T_s + a - \Delta T_v + \Delta T_{v,z} + \Delta T_{n,z}$$

$$= \begin{cases} \Delta T_{v,z} - \Delta T_v + T_{v,L} - c[\exp(m(2L_c - z)) - \exp(mz)] & L_{c,n} \leq z \leq L_c \\ T_{v,L} - T_{L_c} + T_s + a - \Delta T_v + a[\exp(mz) - 1] & 0 \leq z \leq L_{c,n} \end{cases} \quad (3.34)$$

$$m = \left[\frac{2r_o h_c}{k_p (r_o^2 - r_i^2)} \right]^{\frac{1}{2}} \quad (3.35)$$

Eqs. (3.33), (3.34) and (3.35) give the completely closed-form analytical solution of temperature distributions for radially rotating miniature heat pipes with diffuse effects of non-condensable gases. $\Delta T_{v,z}$ in Eq. (3.34) is the vapor temperature drop caused by the friction and centrifugal force along the direction z , which is given by Eq. (3.4). With a low and moderate rotation speed, $\Delta T_{v,z}$ is very small and negligible. ΔT_v in Eq. (3.34) is the total vapor temperature drop along the heat pipe length without the diffuse effects of non-condensable gases, which is calculated by Eq. (2.70). For the heat pipe with fins in the outer surface of the condenser section, r_o may be replaced by the effective radius of outer surface. $T_{v,L}$ and T_v are the temperature at the evaporator end cap and the operating temperature of the heat pipe, respectively. In the normal case, T_v can be replaced by $T_{v,L}$ as the designed heat pipe temperature in the heat pipe design and calculation.

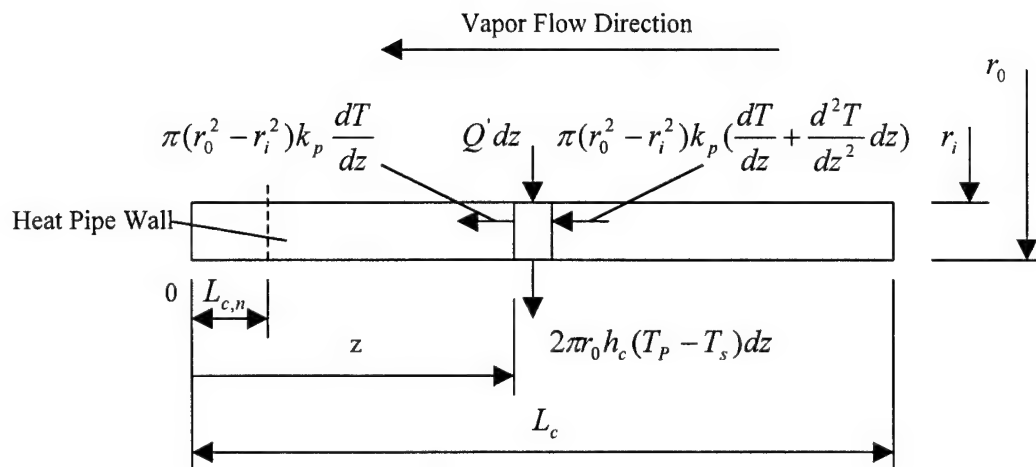


Fig. 3.1 Schematic of diffuse effects of non-condensable gases in the condenser section.

4. HIGH-SPEED ROTATING TEST APPARATUS AND EXPERIMENTAL PROCEDURES

4.1 High-Speed Rotating Test Apparatus and Radially Rotating Miniature Heat Pipes

In order to prove the foregoing analytical results, a high-speed test apparatus and a data acquisition system are constructed. The data acquisition system is shown in Fig. 4.1. The adjustable revolution range of the rotating test apparatus was from 0 to 3,600 rpm, which was controlled by an AC inverter. The maximum working temperature of the miniature heat pipe was 900 °C. An electric heater was used to heat the heat pipe. Its electrical power was adjusted by a transformer from 0 to 120 V, and supplied by a two-channel slip ring. The temperature distributions along the heat pipe were measured by five thermocouples, and fed to a data acquisition system through a 5-channel slip ring. All experimental data, such as heat inputs and temperatures at various locations of the heat pipe, were scanned and recorded by a data acquisition system (HP 34970A, Data Acquisition/Switch Unit), and the data were saved and shown in a computer subsequently.

The high-speed rotating test apparatus is shown in Fig. 4.2. For this particular apparatus, the main parameters which must be controlled in the experiments were the vibration of apparatus, revolutions of the test apparatus, temperatures, heat inputs, and heat dissipation rate of the condenser section along the radially rotating miniature heat pipe. The shaft was driven by a motor [1] with 1 horsepower capacity, in which the motor revolution was varied by from 0 to 3,600 rpm. In order to dampen the vibration of the

rotor, a flexible coupling [18] was used to connect the shaft with the motor. Two ball bearings [6] were selected to fix the position of the shaft. The partial weight of the rotor was transferred to the frame [19] through the bearing house [4] and the 4 sets of springs [3], and the other weight was transferred to the frame [19] through the motor [1] directly. The springs [3] connecting the rotor and frame had some damping function when the rotor system had a slight unbalance and vibration. Therefore, the rotating test apparatus had some self-balance capability. Two slip-ring assemblies [7] were mounted on the shaft. One was used to supply the electrical current from the power transformer to the heater [15] that heated the heat pipe, and the other was used to feed the temperature data from the thermocouples fixed on the heat pipe to the data acquisition system. The rotor disk consisted of an inner cylinder [10] and an outer cylinder [11]. The inner cylinder was mounted on the shaft, and the outer cylinder was fixed on the inner cylinders. In order to prevent the outer and inner cylinder from sliding with respect to each other, two nuts with a bushing were bolted between the inner cylinder and the outer cylinder. The radially rotating miniature heat pipe [14] and a counter weight [9] were mounted on the opposite sides of the outer cylinder in order to balance the rotor system. The heater cap [12] connected on the outer cylinder had two functions: one was to protect the heater, the other was to change the cooling-air flow rate in the condenser through the change of the flow window of cooling air at the heater cap. If the outer diameter of outer cylinder was extended, the rotating radius of the heat pipe could be increased. Thus, the high speed rotating test apparatus would have better versatility so that it can perform a range of experiments with different rotating radii, revolutions, heat inputs, and cooling conditions for the radially rotating miniature heat pipe.

The radially rotating miniature heat pipe is a high-temperature sodium-stainless steel (Type 304W) heat pipe. The compatibility of 304W stainless steel shell with the sodium working fluid has been well documented in the high-temperature heat pipe literature.

Two radially rotating miniature heat pipes were designed to operate at a vapor temperature of about 800 °C in the experiment. One was 1.5 mm in inner diameter, and 80 mm in length, as shown in Fig. 4.3. The other was 2 mm in inner diameter, and 80 mm in length, as shown in Fig. 4.4. To facilitate the sodium charge for these heat pipes, a reservoir with 4 mm in diameter and 3 mm in length was designed on top of the evaporator section with an inner diameter of 1.5 mm. The other reservoir with the same diameter, but 5 mm in length was designed on the top of the evaporator section with an inner diameter of 2 mm. The end cap was welded on the reservoir of the evaporator section, and a filling tube with an outer diameter of 2.1 mm was welded onto the end cap. Two radially rotating miniature heat pipes had the same outer diameter, 6 mm, and the same evaporator and condenser lengths, 40 mm, respectively. Four fins were made on the outer surface of the condenser section in order to increase the convective heat transfer on the outer surface of the condenser section. The heat pipes and heater caps were fabricated from Type 304W stainless steel. The screw thread was machined on the heat pipe root so that the heat pipe could be screwed into the outer cylinder of the high speed rotating test apparatus. All of the heat pipe parts were carefully fitted and cleaned according to standard procedures. The heat pipes and end caps were degreased with 1,1,1-trichloroethane, rinsed in tap water, then rinsed in methanol and allowed to air dry. The

welding process of filling tubes, end caps and heat pipes were protected from oxidation by a cover layer of the argon.

The sodium charge in the radially rotating miniature heat pipes was processed by THERMACORE INC., PA. The processing procedure was as follows:

- 1) Sodium was charged into the heat pipes in an argon-filled glove box.
- 2) The open ends of the heat pipes were attached to a turbo-pump vacuum station.
- 3) While pumped at a high vacuum level, heat pipes were heated to 100-200 °C to drive off any absorbed water and atmospheric gases.
- 4) The filling tubes of the heat pipes were pinched and welded if the vacuum in the box remained at a high vacuum level.

For the radially rotating miniature heat pipe with an inner diameter of 1.5 mm, the sodium charge was approximately 0.06 g, and 0.08 g of sodium was charged into the other radially rotating miniature heat pipe with an inner diameter of 2 mm.

There were five thermocouples of type K used to measure the heat pipe temperature distributions along the heat pipe length, which were calibrated with a accuracy of ± 0.5 °C by the OMEGA ENGINEERING INC. Two thermocouples were installed in the evaporator section to measure the temperatures in the evaporator section, and other three thermocouples were mounted in the condenser section to measure the temperatures of the condenser section. These five thermocouple heads were inserted into five small holes of diameter of 0.8 mm in the heat pipe shell along the heat pipe length, and were fixed firmly on the outer surface of the heat pipe.

The heater was made of the high temperature chemical set cement, OMEGABOND "600", and the Nickel-Chromium alloy resistance heating wires, NI80-010 or NI80-012, from OMEGA ENGINEERING INC. The procedure for the fabrication of the heater was as follows:

- 1) Mixing 100 parts of the high temperature chemical set cement with 13 parts water by weight.
- 2) Painting a thin layer of the mixture on the outer surface of the heat pipe uniformly.
- 3) Wrapping the Nickel-Chromium alloy resistance heating wire on the surface of the cement as a heating coil after the high temperature chemical set cement cures with an internal chemical-setting action in 18-24 hours at ambient temperature or 4 hours at 180-220 °F.
- 4) Painting another thick layer of the mixture on the heating coil.

The heater was mounted on the outer surface of the evaporator section firmly, and the insulation material of about 16 mm in thickness was stuffed between the heater and heater cap to make sure that the heat from the heater could be transferred into the evaporator section of the heat pipe effectively.

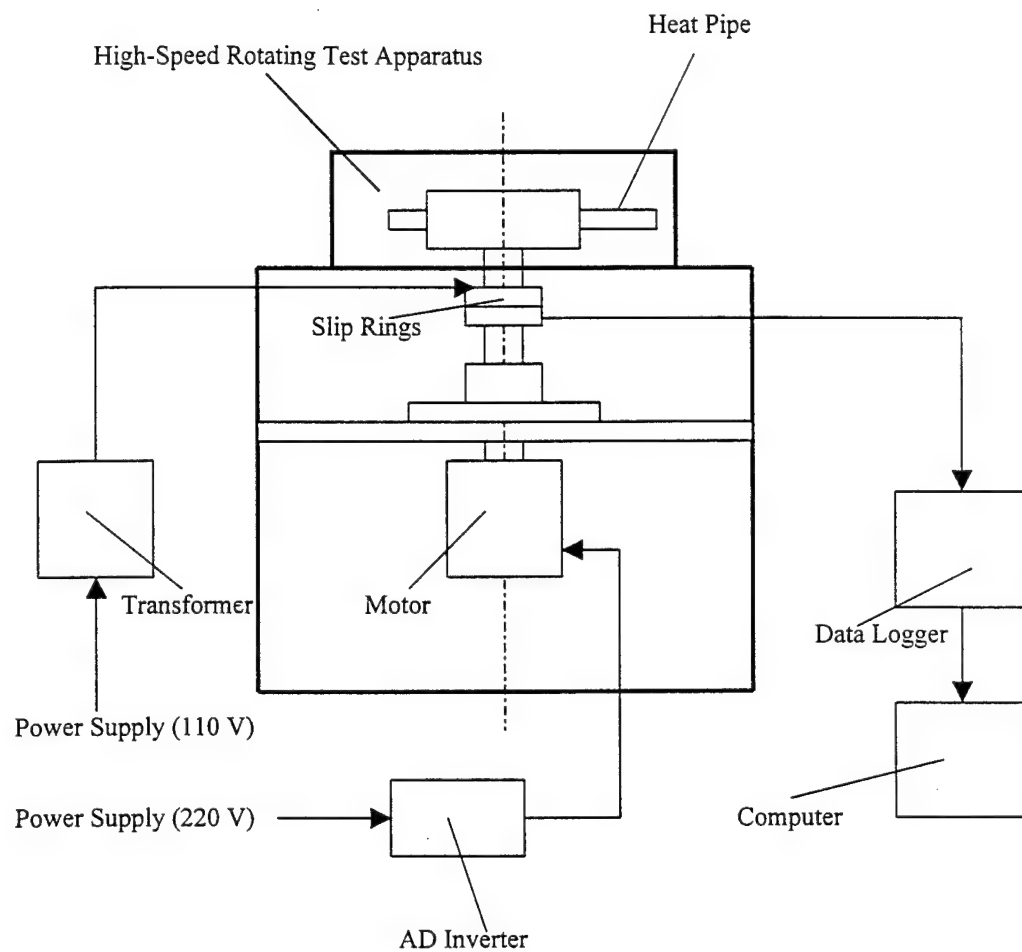
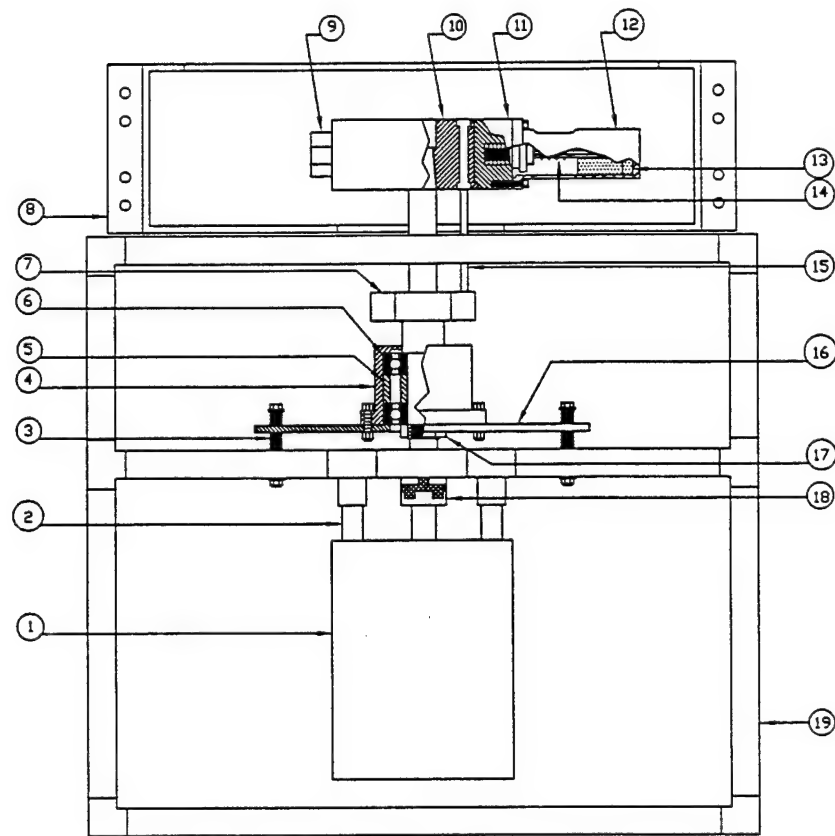


Fig. 4.1 Schematic of a high-speed rotating test apparatus and data acquisition system.



1	Motor	8	Protective Shell	15	Thermocouples
2	Connecting Bar	9	Balancing Weight	16	Bearing Platform
3	Springs	10	Inner Cylinder	17	Bearing Nut
4	Bearing House	11	Outer Cylinder	18	Flexible Coupling
5	Spacer	12	Heater Cap	19	Frame
6	Bearing	13	Heater		
7	Slip Rings	14	Heat Pipe		

Fig. 4.2 Schematic of the high speed rotating test apparatus.

Material: 304 Stainless Steel.

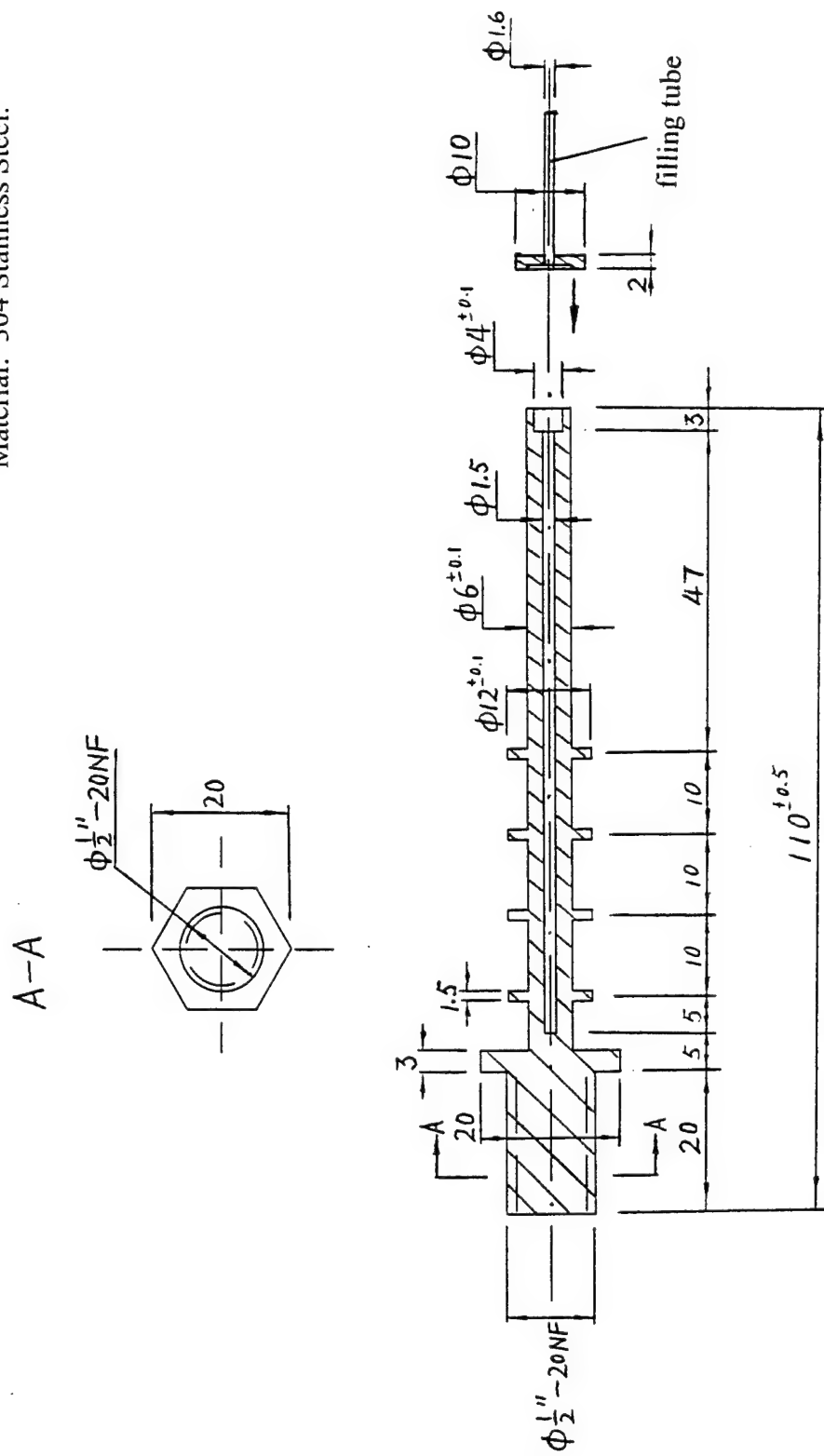


Fig. 4.3 Schematic of radially rotating miniature heat pipe with a inner diameter of 1.5 mm.

Material: 304 Stainless Steel.

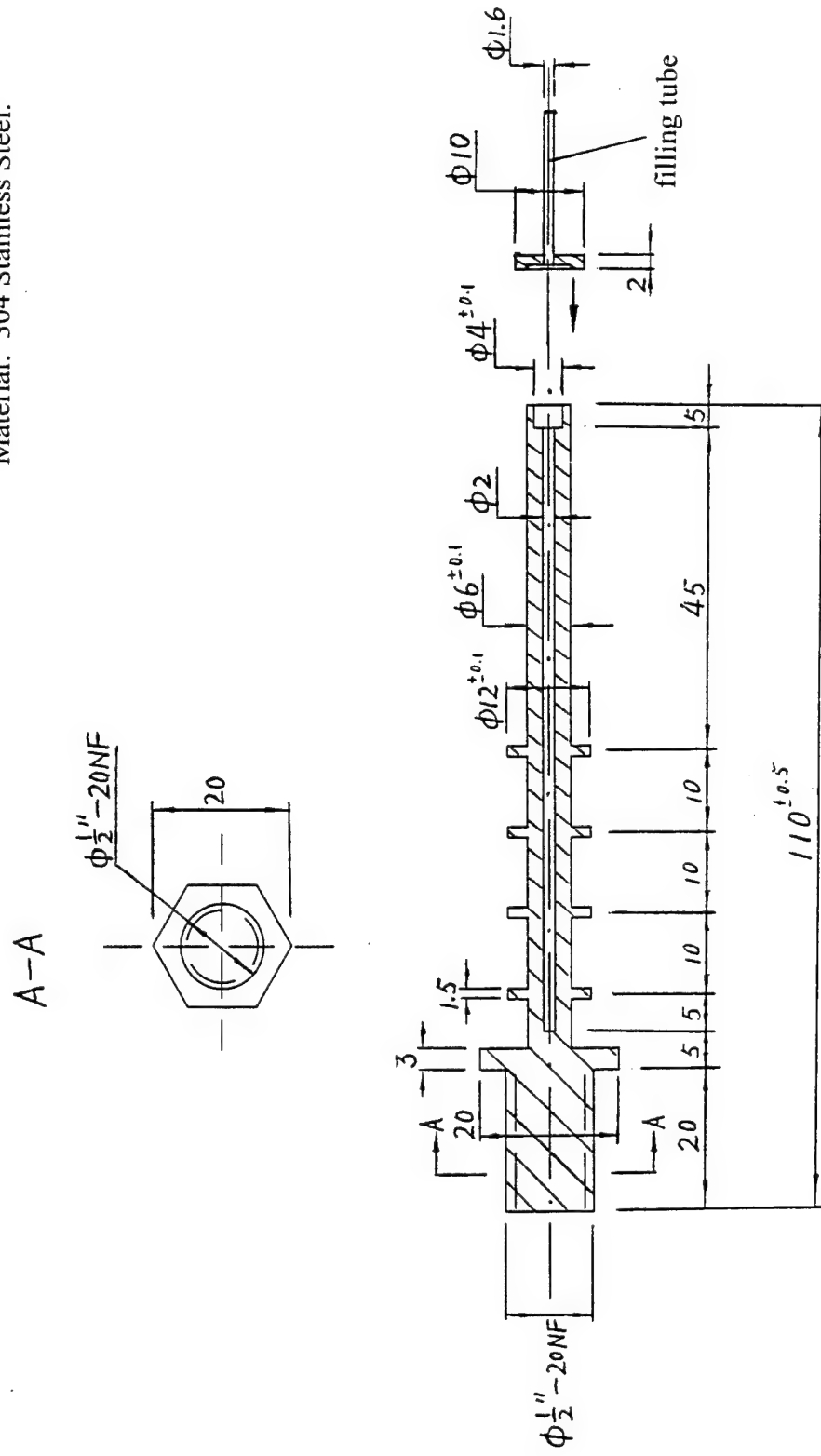


Fig. 4.4 Schematic of radially rotating miniature heat pipe with a inner diameter of 2 mm.

4.2 Experimental Results and Analyses

According to the foregoing analysis of flow and heat transfer for the liquid film and vapor in a radially rotating miniature heat pipe, it can be found that the temperature drop and the temperature distribution along the heat pipe length are the function of rotating speed, heat pipe length, heat pipe inner diameter, working fluid properties, tilt angle, heat input in the evaporator section, and cooling condition in the condenser section. At the same time, other parameters such as non-condensable gases existing in the heat pipe and heat conductivity of the heat pipe container material also have a distinct influence on the temperature distribution and heat transfer in the heat pipe.

In the experiments for the radially rotating miniature heat pipe, the tilt angle, ϕ , of the heat pipe is designed as 90° . The ranges of heat inputs, geometric dimensions, flow rates of cooling air, and rotating speeds or frequencies are as follows:

$47 \text{ W} \leq Q \leq 325 \text{ W}$, $d_i = 1.5 \text{ mm}$ and 2 mm , $L = 80 \text{ mm}$, $L_c = L_e = 40 \text{ mm}$, $L_a = 0$, $1.05 \times 10^{-3} \text{ m}^3/\text{s} \leq W \leq 13.4 \times 10^{-3} \text{ m}^3/\text{s}$, $470 \leq \omega^2 \bar{Z}_a / g \leq 1881$, $30 \text{ Hz} \leq f \leq 60 \text{ Hz}$. In the following, experimental data are presented in terms of the following five aspects.

4.2.1 Operating Characteristics of High-Temperature Radially Rotating Miniature Heat Pipes

As mentioned earlier, there are many influential factors for the operation of high-temperature radially rotating miniature heat pipe. The major factors are the heat input in the evaporator section, flow rate of the cooling air in the condenser section, heat pipe size, and dimensionless centrifugal force and non-condensable gases in the heat pipe.

To illustrate the effectiveness of the heat pipe, Table 4.1 and Fig. 4.5 show the comparisons of the temperature distributions along a heat pipe and those along a heat pipe container (the heat pipe shell without charging any fluid) with the same flow rate of cooling air, dimensionless centrifugal forces, and geometrical dimensions. From Table 4.1 and Fig. 4.5, it can be seen that the heat transfer capacity of the heat pipe container is very low, which is 47 W for the heat pipe container with an inner diameter of 2 mm, and 60 W for that of 1.5 mm. The temperature distributions along most of the container length are approximately linear, and temperature in the portion near the condenser end is close to the temperature of the cooling air. For the heat pipes with the same flow rate of cooling air, dimensionless centrifugal force, and geometrical dimensions, much more heat can be transferred, which is up to 280 W for the heat pipe with an inner diameter of 2 mm, and 250 W for that of 1.5 mm. If the thermal conductivity for the copper is $386 \text{ W/m}^\circ\text{C}$, the effective thermal conductance of the heat pipes is 60 - 100 times higher than the thermal conductivity of copper. These comparisons prove that high-temperature radially rotating miniature heat pipes can work very effectively. Their heat transfer characteristics are much better than any metals.

Temperature distributions along the evaporator section and most portion of the condenser section are almost uniform. It shows that the heat pipe works perfectly in these sections. But there exists a larger temperature gradient near the end cap of the condenser. This is because the condenser end is fixed on the outer cylinder of the high-speed rotating test apparatus with a screw thread, an extra heat sink is formed at the condenser end, and more heat from the condenser end is transferred into the heat sink. As a result, because of the heat sink at the condenser end, the temperature distribution close to the condenser end is lowered.

Table 4.2 and Fig. 4.6 give the temperature distributions along the heat pipe length in the process of the heat pipe startup. At $t=0$, a heat input, $Q=176$ W, is applied suddenly to the evaporator section through the heater described early for the heat pipe with an inner diameter of 1.5 mm, and $Q=175$ W for the other heat pipe with an inner diameter of 2 mm. At this moment, the temperatures along the heat pipe length are the same, and the temperature distribution along the heat pipe length is a straight line because of the retardation of the heat transfer from the heater, as shown in Fig. 4.6. With the increase in time, the temperature in the outlet of the evaporator section rises faster than that near the end cap of the evaporator, and temperatures along the condenser section almost keep constant. Because the evaporator end has a larger metal mass and holds almost all the solid sodium, it needs to absorb more heat to raise its temperature. In general, this phenomenon, in which the temperature at the outlet of the evaporator section is higher than that at the end cap of the evaporator, lasts only about 60 seconds. After that time, the temperature at the end cap of the evaporator is higher than that at the outlet of the evaporator section, and temperature along the condenser section increases gradually

because the end cap of the evaporator is insulated and the heat from the outlet of the evaporator section is transferred to the condenser section by the axial heat conduction along the container wall. As the temperature in the evaporator section is further increased, the sodium in the evaporator section is evaporated, vapor flows from the evaporator section to the condenser section, and the heat pipe begins working. The temperatures along the heat pipe length rise quickly. After about 1200 -1800 seconds, the temperature distribution along the heat pipe length reaches a steady state and the process of the heat pipe startup is completed.

At a lower heat input, the heat pipe could not work since the operating temperature in the evaporator section is too low and the sodium may remain to be solid and would not evaporate. When the heat input is increased, the evaporator section of the heat pipe starts to work first. But the vapor generated in the evaporator section will be condensed quickly near the condenser inlet, and condensate will return to the evaporator section under the action of the centrifugal force if the flow rate of the cooling air in the condenser section is high enough. As the heat input in the evaporator section is further increased, the front of vapor flow from the evaporator section will move forward towards the end of the condenser section, and the working section in the condenser will be increased gradually.

Fig. 4.7 illustrates the steady state operation of two radially rotating miniature high-temperature heat pipes with inner diameters of 1.5 and 2 mm when the dimensionless centrifugal force is 470, the flow rate of the cooling air is $0.0067 \text{ m}^3/\text{s}$, and the temperature of the cooling air is about 30°C . From Fig. 4.7, it is clear that the evaporator sections of the heat pipes start to work, and the temperature distributions in

the evaporator section are almost uniform when the heat input reaches 100 W. Because the working sections in the condensers are relative short, the temperatures in the condenser section drop sharply so that the temperatures near the condenser end are almost close to the cooling air temperature. With the increase of heat inputs, the operating temperatures in the evaporator sections will rise, and vapor flow rates from the evaporator sections will increase. At the same time, the working sections in the condensers will be extended towards the condenser end, and the temperature along the condenser section will go up quickly. When the heat input approaches about 280 W for the heat pipe with an inner diameter of 2 mm, and 250 W for that of 1.5 mm, the temperature distributions in the evaporator sections and most parts of the condenser sections are almost uniform. However, the temperature gradient near the end of the condenser section still remains high due to the diffuse effects of non-condensable gases and heat sink at the condenser end.

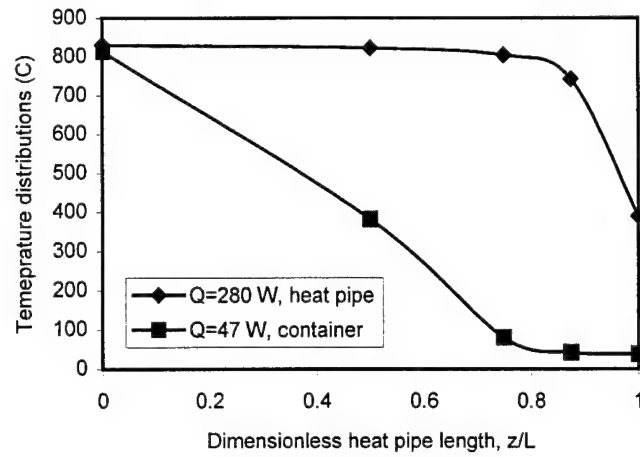
Table 4.1 Comparisons of heat pipes and heat pipe containers with the same geometry.

(a) $\omega^2 \bar{Z}_a / g = 470$, $d_i = 2$ mm, $W = 6.7 \times 10^{-3} \text{ m}^3 / \text{s}$, $Q = 280$ W for the heat pipe and $Q = 47$ W for the heat pipe container

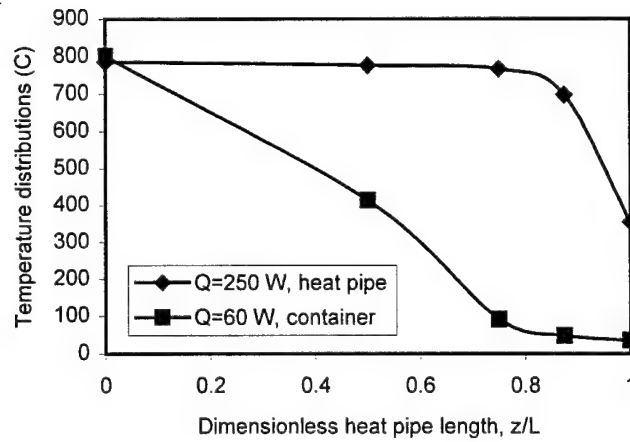
Dimensionless heat pipe length z/L	Temp. distributions for the heat pipe ($^{\circ}\text{C}$)	Temp. distributions for the heat pipe container ($^{\circ}\text{C}$)
0.000	830.0	814.2
0.500	821.8	382.1
0.750	804.4	79.5
0.875	742.4	42.0
1.000	390.0	37.9

(b) $\omega^2 \bar{Z}_a / g = 470$, $d_i = 1.5$ mm, $W = 6.7 \times 10^{-3} \text{ m}^3 / \text{s}$, $Q = 250$ W for the heat pipe and $Q = 60$ W for the heat pipe container

Dimensionless heat pipe length z/L	Temp. distributions for the heat pipe ($^{\circ}\text{C}$)	Temp. distributions for the heat pipe container ($^{\circ}\text{C}$)
0.000	786.0	801.5
0.500	776.4	413.5
0.750	766.2	91.8
0.875	698.4	48.2
1.000	354.3	35.3



(a) $\omega^2 \bar{Z}_a / g = 470$, $d_i = 2$ mm, $W = 6.7 \times 10^{-3}$ m³/s



(b) $\omega^2 \bar{Z}_a / g = 470$, $d_i = 1.5$ mm, $W = 6.7 \times 10^{-3}$ m³/s

Fig. 4.5 Comparisons of temperature distributions between the heat pipe and the heat pipe container.

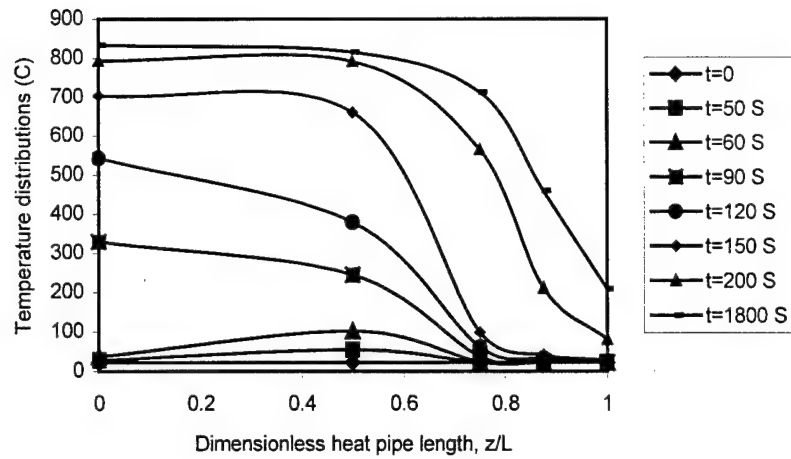
Table 4.2 Temperature distributions along the heat pipe length with the diffuse effects of non-condensable gases during the heat pipe startup process.

(a) $\omega^2 \bar{Z}_a / g = 470$, $d_i = 1.5$ mm, $Q = 176$ W

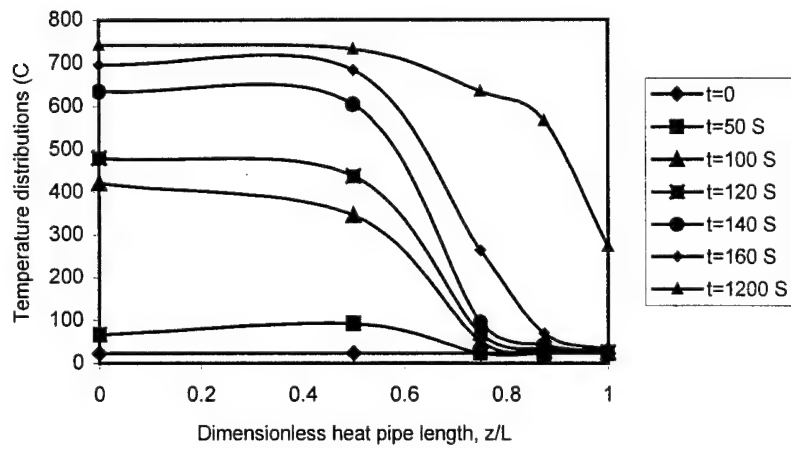
	$z/L=0$	$z/L=0.5$	$z/L=0.75$	$z/L=0.875$	$z/L=1$
$t=0$	22 °C	22 °C	22 °C	22 °C	22 °C
$t=50$ S	28 °C	54 °C	22 °C	22 °C	22 °C
$t=60$ S	37 °C	101 °C	24 °C	22 °C	22 °C
$t=90$ S	329 °C	244 °C	37 °C	25 °C	22 °C
$t=120$ S	543 °C	379 °C	61 °C	32 °C	23 °C
$t=150$ S	704 °C	671 °C	98 °C	41 °C	27 °C
$t=200$ S	794 °C	792 °C	564 °C	211 °C	81 °C
$t=1800$ S	834 °C	816 °C	713 °C	460 °C	208 °C

(b) $\omega^2 \bar{Z}_a / g = 470$, $d_i = 2$ mm, $Q = 175$ W

	$z/L=0$	$z/L=0.5$	$z/L=0.75$	$z/L=0.875$	$z/L=1$
$t=0$	23 °C	23 °C	23 °C	23 °C	23 °C
$t=50$ S	66 °C	92 °C	24 °C	23 °C	23 °C
$t=100$ S	421 °C	346 °C	51 °C	29 °C	25 °C
$t=120$ S	480 °C	438 °C	70 °C	35 °C	26 °C
$t=140$ S	635 °C	605 °C	96 °C	42 °C	28 °C
$t=160$ S	696 °C	684 °C	264 °C	70 °C	32 °C
$t=1200$ S	742 °C	732 °C	635 °C	567 °C	273 °C

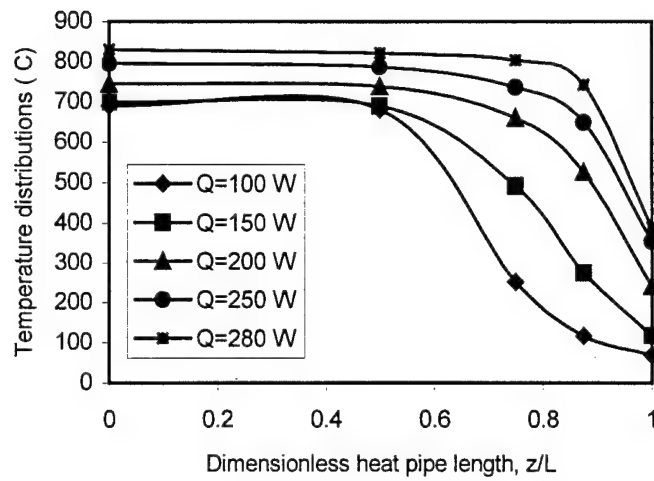


(a) $\omega^2 \bar{Z}_a / g = 470$, $d_i = 1.5$ mm, $Q = 176$ W

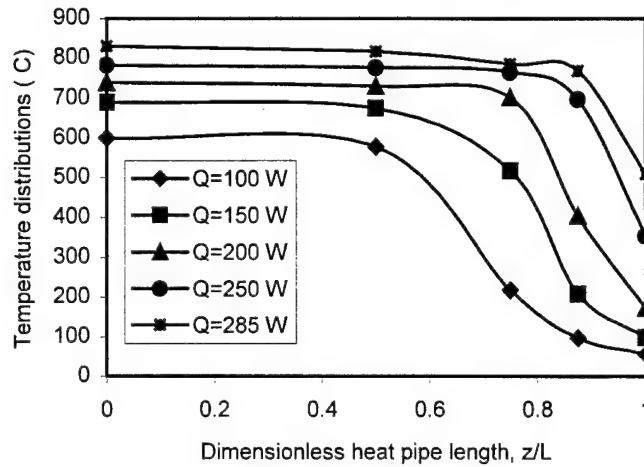


(b) $\omega^2 \bar{Z}_a / g = 470$, $d_i = 2$ mm, $Q = 175$ W

Fig. 4.6 Temperature distributions along the dimensionless heat pipe length with the diffuse effects of non-condensable gases during the heat pipe startup process.



(a) $\omega^2 \bar{Z}_a / g = 470$, $d_i = 2$ mm, $W = 6.7 \times 10^{-3}$ m³/s



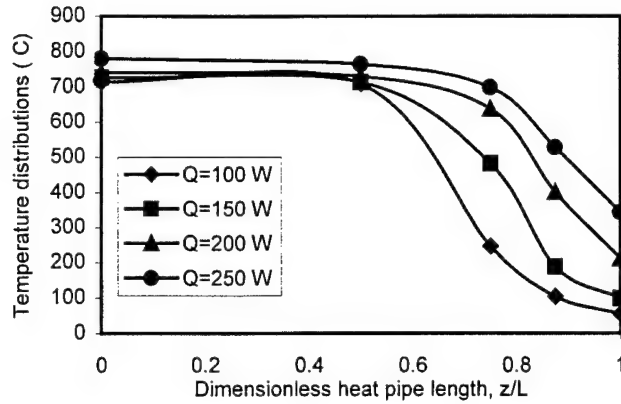
(b) $\omega^2 \bar{Z}_a / g = 470$, $d_i = 1.5$ mm, $W = 6.7 \times 10^{-3}$ m³/s

Fig. 4.7 Temperature distributions along the dimensionless heat pipe length with different heat inputs.

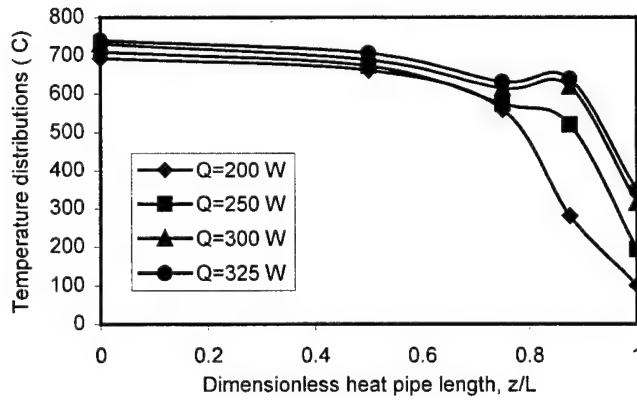
4.2.2 Effects of Heat Inputs

As mentioned earlier, the heat input has a very important influence on the temperature distributions and heat transfer characteristics of the heat pipes. When the flow rate of cooling air, dimensionless centrifugal force, and inner diameters of the heat pipes are fixed, with an increase in heat inputs, the operating temperatures in the evaporator section will rise, and the temperature distributions along the condenser section will go up quickly, as shown in Figs. 4.8 and 4.9. Accordingly, the heat transfer characteristics and effective thermal conductance will be improved greatly. If the flow rate of the cooling air and dimensionless centrifugal force are fixed and the heat input reaches 300 W for the heat pipe with an inner diameter of 2 mm, and 285 W for that of 1.5 mm, the temperature distribution along the heat pipe length stays relatively uniform until reaching the region close to condenser end. But a temperature peak occurs near the condenser end, as shown in Figs. 4.8(b) and 4.9(a). This is because with the increase of heat inputs, a lot of vapor is generated in the evaporator sections. If the flow rate of cooling air, dimensionless centrifugal force, and geometrical dimensions of heat pipes are fixed, more vapor would flow towards the end of the condenser section. There, the velocity of vapor is reduced to zero, and the vapor kinetic energy is converted into the thermal energy which causes the vapor pressure and temperature to rise again. Owing to the effect of non-condensable gases and the heat sink at the condenser end, the temperature at the condenser end is still relative low. As a result, a temperature peak would appear close to the end of the condenser section.

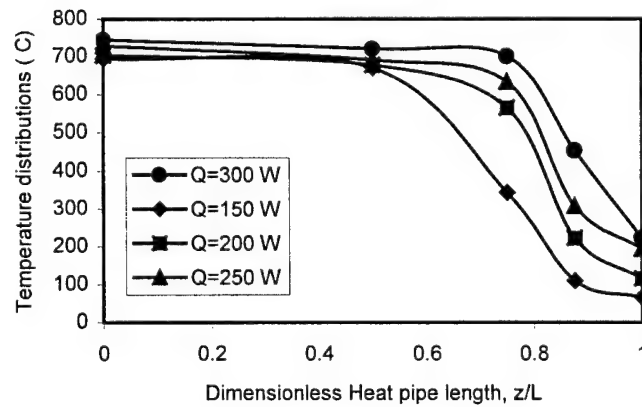
The heat transfer rate of the heat pipe can be changed with different flow rates of cooling air and dimensionless centrifugal forces if the heat input and geometrical dimensions of the heat pipe are kept at a constant. As the dimensionless centrifugal force and flow rate of the cooling air are increased, the film thickness of condensate on the inner wall of the condenser will decrease and the cross-section area of the vapor flow passage will be enlarged. As a result, the heat transfer between the vapor and inner wall of the condenser will be enhanced. At the same time, as a result of the increased flow rate of the cooling air, much more heat will be carried away from the condenser section. Therefore, the vapor from the evaporator section can condense more effectively in the condenser section without raising the temperature in that region. Figs. 4.8(c) and 4.9(c) show that the temperature peak for heat pipes with the same inner diameters has disappeared. Compared to the temperature distributions in Fig. 4.8(b) and 4.9(a), the temperature distributions except those near the condenser end in Fig. 4.8(c) and 4.9(c) becomes smoother because of a larger flow rate of the cooling air.



(a) $\omega^2 \bar{Z}_a / g = 470$, $d_i = 2$ mm, $W = 6.7 \times 10^{-3}$ m³/s

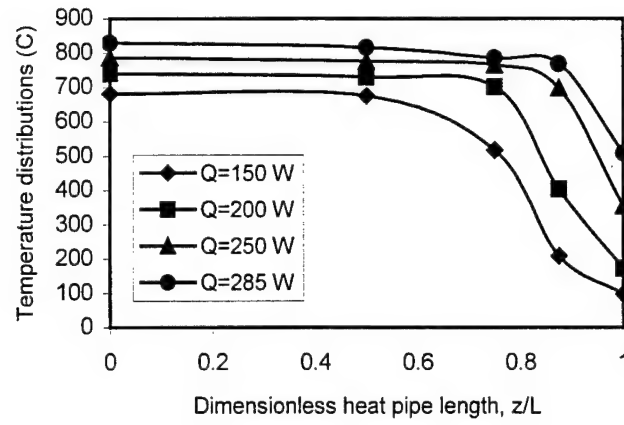


(b) $\omega^2 \bar{Z}_a / g = 1306$, $d_i = 2$ mm, $W = 11.2 \times 10^{-3}$ m³/s

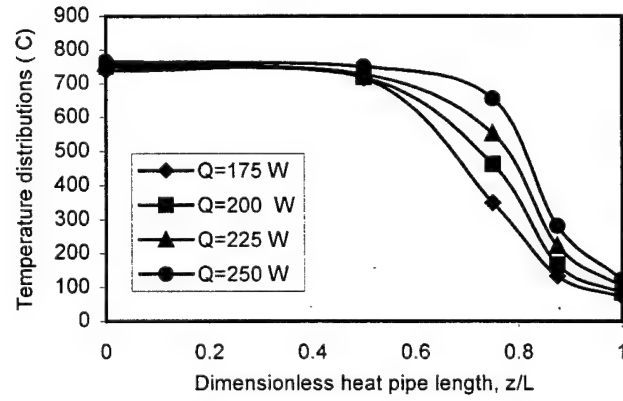


(c) $\omega^2 \bar{Z}_a / g = 1881$, $d_i = 2$ mm, $W = 13.4 \times 10^{-3}$ m³/s

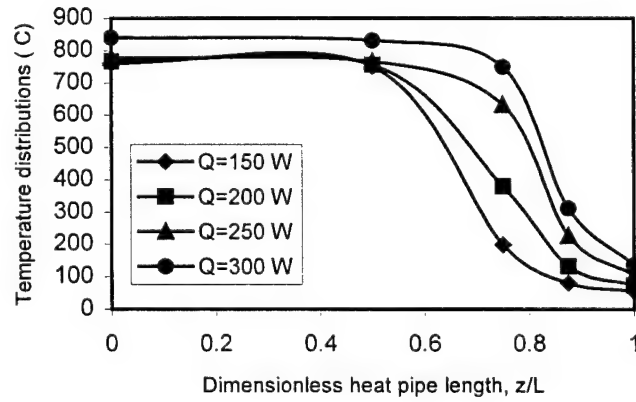
Fig. 4.8 Temperature distributions along dimensionless heat pipe length the with different rotating frequencies and flow rates of the cooling air.



(a) $\omega^2 \bar{Z}_a / g = 470$, $d_i = 1.5$ mm, $W = 6.7 \times 10^{-3}$ m³/s



(b) $\omega^2 \bar{Z}_a / g = 1306$, $d_i = 1.5$ mm, $W = 11.2 \times 10^{-3}$ m³/s



(c) $\omega^2 \bar{Z}_a / g = 1881$, $d_i = 1.5$ mm, $W = 13.4 \times 10^{-3}$ m³/s

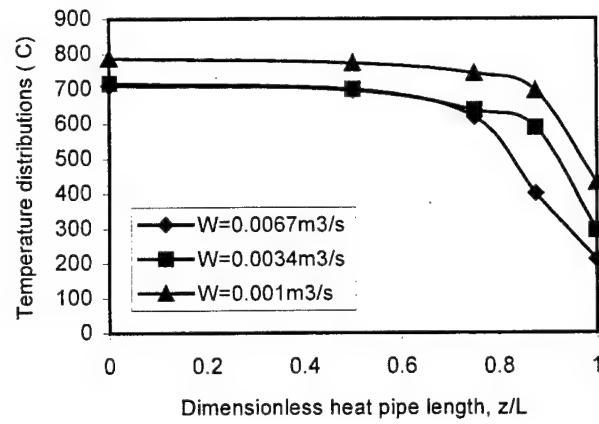
Fig. 4.9 Temperature distributions along the dimensionless heat pipe length with different rotating frequencies and flow rates of the cooling air.

4.2.3 Effects of the Cooling Air Flow Rates

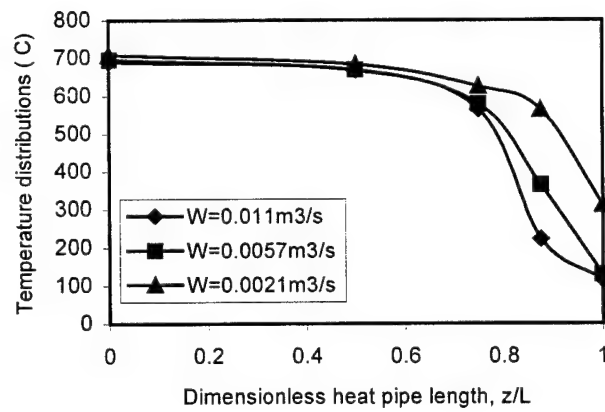
Flow rate of the cooling air in the condenser section has a dominant influence on the operating temperature level of the heat pipe. As the flow rate of the cooling air is increased, the convective heat transfer on the outer surface of the condenser section will increased, and more vapor can be condensed in the condenser section. Therefore, the heat transfer capacity of the heat pipe will increase. Accordingly, if the heat input keeps a constant, with the cooling air flow rate in increase, the operating temperature of the heat pipe will be lower, the working section of the condenser will be shorter, and the temperature distributions along the condenser section will be less uniform near the condenser end.

Figs. 4.10 and 4.11 compare the temperature distributions along the dimensionless heat pipe length with the same heat input, dimensionless centrifugal force, and the cooling air temperature when the flow rate of the cooling air, W , is changed from $0.001 \text{ m}^3/\text{s}$ to $0.011 \text{ m}^3/\text{s}$ through the change of the flow window of the cooling air on the heat pipe cap. From Figs. 4.10 and 4.11, it can be seen that, for the same heat input and dimensionless centrifugal force, the temperature distributions along dimensionless heat pipe length rise with a decrease in the flow rates of the cooling air. Because at a higher flow rate of the cooling air, the operating temperature level of the heat pipe is reduced. Accordingly, the vapor pressure level in the heat pipe is reduced. Due to this reduced vapor pressure, the viscosity of the condensate is increased, and the vapor flow resistance on the liquid-vapor interface will rise. Therefore, the temperature drop caused by the friction will be increased. At the same time, the non-condensable gases in the heat pipe is

less likely to be compressed towards the condenser end owing to the reduced vapor pressure. As a result, the non-condensable gases would occupy a larger portion of the condenser section, the temperature distribution near the condenser end becomes less uniform, and the temperature gradient is steeper near the condenser end.

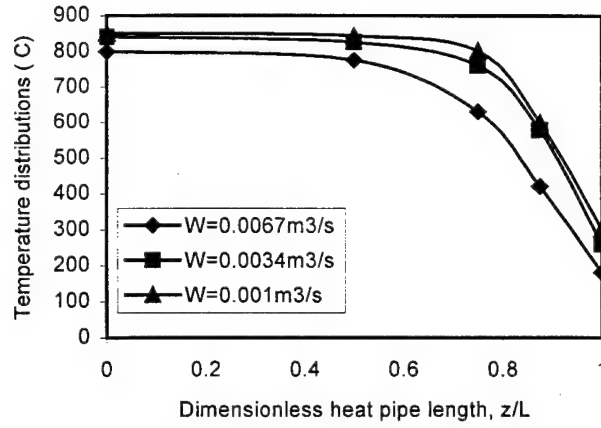


(a) $\omega^2 \bar{Z}_a / g = 470$, $d_i = 2 \text{ mm}$, $Q = 200 \text{ W}$

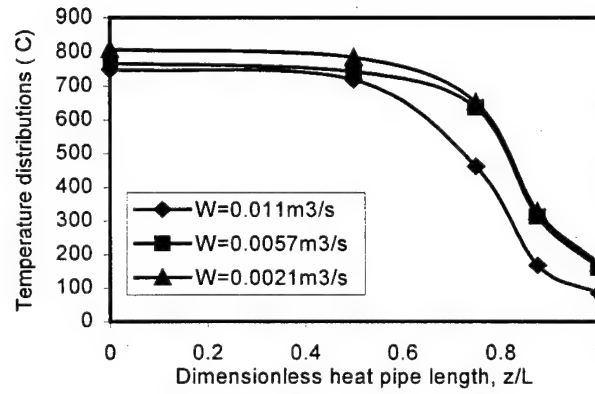


(b) $\omega^2 \bar{Z}_a / g = 1306$, $d_i = 2 \text{ mm}$, $Q = 200 \text{ W}$

Fig. 4.10 Comparisons of temperature distributions along dimensionless heat pipe length with different flow rates of the cooling air.



(a) $\omega^2 \bar{Z}_a / g = 470$, $d_i = 1.5 \text{ mm}$, $Q = 200 \text{ W}$



(b) $\omega^2 \bar{Z}_a / g = 1306$, $d_i = 1.5 \text{ mm}$, $Q = 200 \text{ W}$

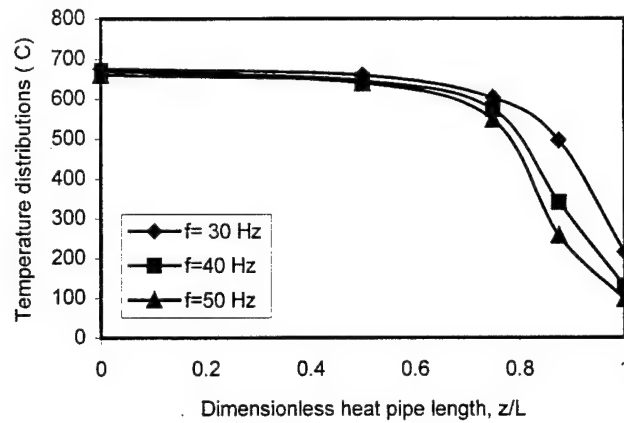
Fig. 4.11 Comparisons of temperature distributions along dimensionless heat pipe length with different flow rates of the cooling air.

4.2.4 Effects of Dimensionless Centrifugal Forces

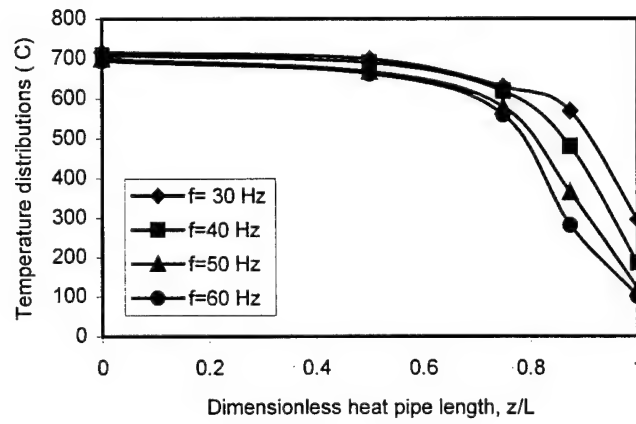
As mentioned in the foregoing analyses in chapter 2, at a higher revolution or rotating frequency, the dimensionless centrifugal force plays a dominant role in the total temperature drop along the heat pipe length. With an increase in the dimensionless centrifugal force, the pressure and temperature drops along the heat pipe length will be increased if heat inputs and geometrical dimensions of the heat pipe are fixed. Therefore, to some degree, the dimensionless centrifugal force dominates the slope of temperature distribution and the total temperature drop along dimensionless heat pipe length.

Though the dimensionless centrifugal force has a similar trend for the total temperature drop along the heat pipe length compared to the flow rate of the cooling air, the mechanism causing the change of the temperature drop is different. As the cooling air flow rate is increased, the convection on the outer surface of the condenser section will be intensified, the working section in the condenser will be shorted, and the temperature distribution along the condenser length will become steeper if the heat input keeps a constant. But the slope of the temperature distribution along the evaporator section will keep a constant. As a result, the total temperature drop along the heat pipe length is increased. While the dimensionless centrifugal force is increased, the temperature drop caused by the vapor centrifugal force will rise, and the total temperature drop along the heat pipe length will be increased. Accordingly, it results in the increase of the slope of the temperature distribution along the heat pipe length. Therefore, the analysis here is limited to the slope of temperature distributions along the evaporator section in order to illustrate the effects of dimensionless centrifugal forces.

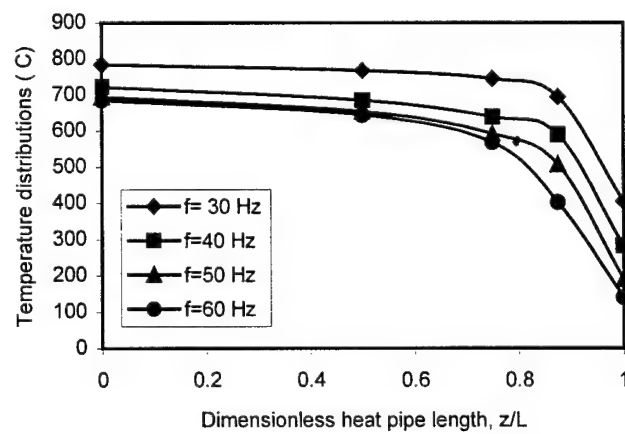
Figs. 4.12 and 4.13 show temperature distributions along dimensionless heat pipe length when heat inputs and geometrical dimensions are fixed and the dimensionless centrifugal force, $\omega^2 \bar{Z}_a / g$, is changed from 470 to 1881. As shown in Figs. 4.12 and 4.13, at a low rotating frequency, $f=30$ Hz, which corresponds to a dimensionless centrifugal force, $\omega^2 \bar{Z}_a / g$, of 470, the slopes of the temperature distributions along the evaporator section are relatively small, and temperature distributions along the evaporator section are relatively uniform. When the rotating frequency and dimensionless centrifugal force are increased, the slopes of temperature distributions along the evaporator section become steeper with an increased temperature drop in the evaporator section. As can be seen, at a higher rotating frequency of $f=60$ Hz, corresponding to $\omega^2 \bar{Z}_a / g=1881$, the slopes of the temperature distributions and the temperature drops along the evaporator section are relatively high. With a further increase in rotating frequencies and dimensionless centrifugal forces, the trend will be more evident.



(a) $Q=175$ W, $d_i=2$ mm

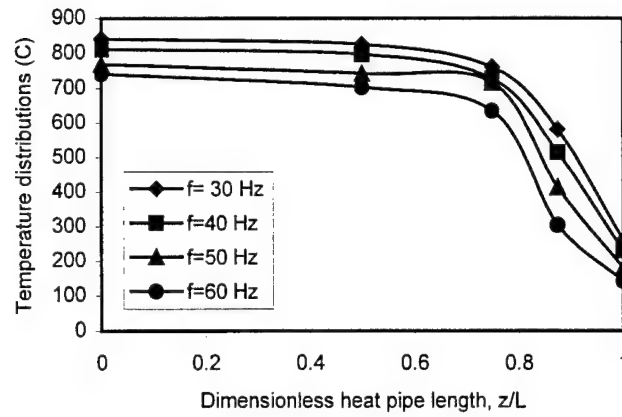


(b) $Q=200$ W, $d_i=2$ mm

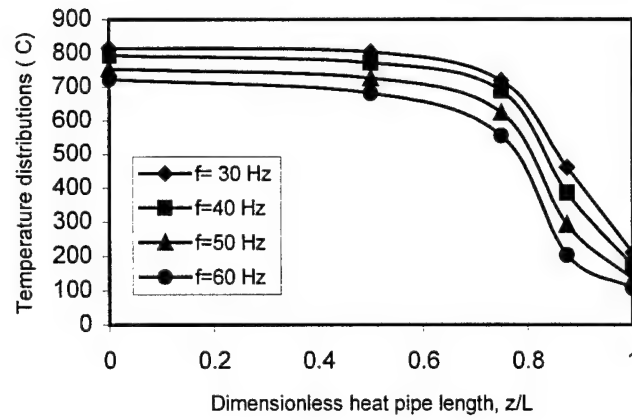


(c) $Q=225$ W, $d_i=2$ mm

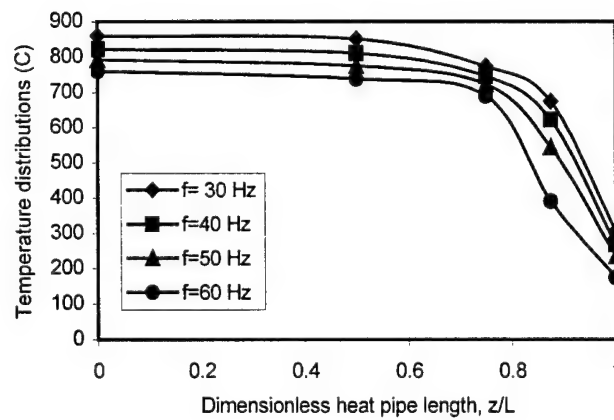
Fig. 4.12 Temperature distributions along the dimensionless heat pipe length with different rotating frequencies.



(a) $Q=175$ W, $d_i=1.5$ mm



(b) $Q=200$ W, $d_i=1.5$ mm



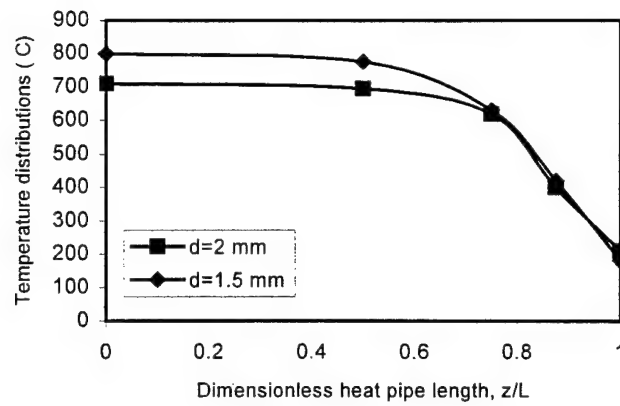
(c) $Q=225$ W, $d_i=1.5$ mm

Fig. 4.13 Temperature distributions along the dimensionless heat pipe length with different rotating frequencies.

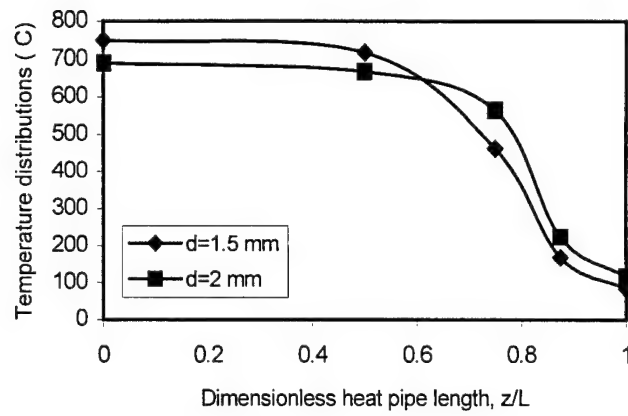
4.2.5 Effects of Inner Diameters of the Heat Pipes

The inner diameter of a heat pipe determines the cross-sectional area of vapor flow in the heat pipe. For a radially rotating miniature heat pipe, if it has a relatively larger inner diameter, the friction of vapor flow is relatively smaller. As a result, the temperature drop caused by the friction of the vapor flow is smaller. Conversely, a radially rotating miniature heat pipe having a smaller inner diameter must have a larger friction of vapor flow and a larger temperature drop in the heat pipe. This phenomenon has been analyzed and predicted in details in chapter 2. The experimental evidence will be presented in this chapter.

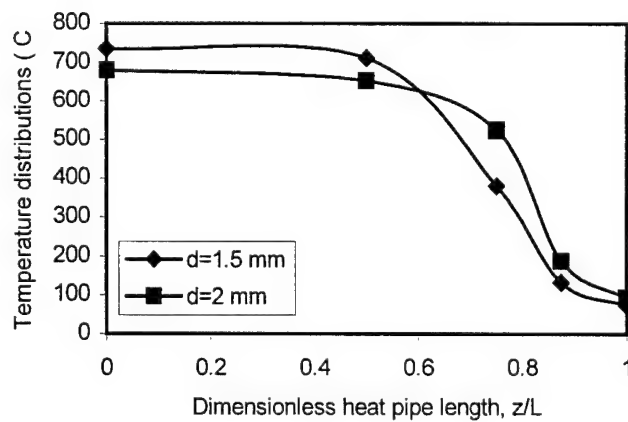
Figs. 4.14 and 4.15 show the comparisons of temperature distributions along the dimensionless heat pipe length for heat pipes with inner diameters of 2 mm and 1.5 mm. It is evident that the temperature drops along the heat pipe with an inner diameter of 1.5 mm are larger than those with an inner diameter of 2 mm when the heat input, dimensionless centrifugal force, and flow rate of cooling air are kept at constants. On the other hand, the operating temperature in the evaporator section of the heat pipe having an inner diameter of 1.5 mm is higher than that of 2 mm. This is because a higher pressure drop is needed to overcome the friction of vapor flow in the heat pipe with an inner diameter of 1.5 mm. Therefore, the vapor pressure in the evaporator section of the heat pipe with the inner diameter of 1.5 mm is higher than that of 2 mm. Accordingly, the saturated temperature in the evaporator section of the heat pipe having an inner diameter of 1.5 mm is higher than that of 2 mm. This trend will be more evident with a further decrease in the inner diameter of the heat pipe.



(a) $Q=200 \text{ W}, \omega^2 \bar{Z}_a / g = 470$

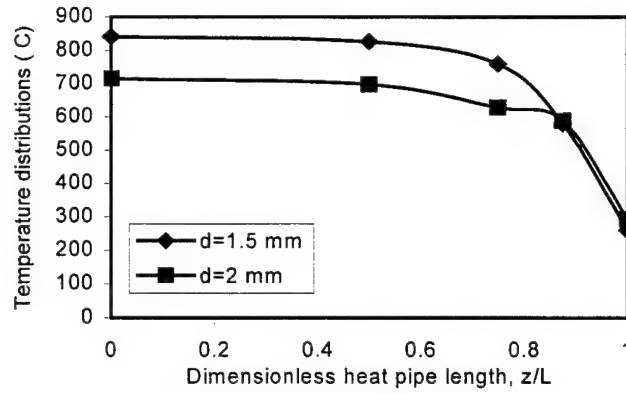


(b) $Q=200 \text{ W}, \omega^2 \bar{Z}_a / g = 1306$

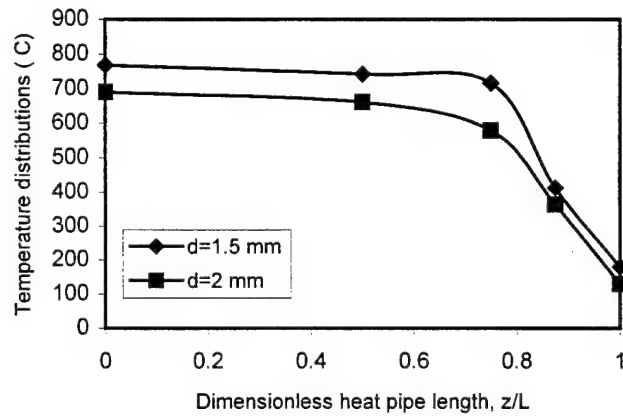


(c) $Q=200 \text{ W}, \omega^2 \bar{Z}_a / g = 1881$

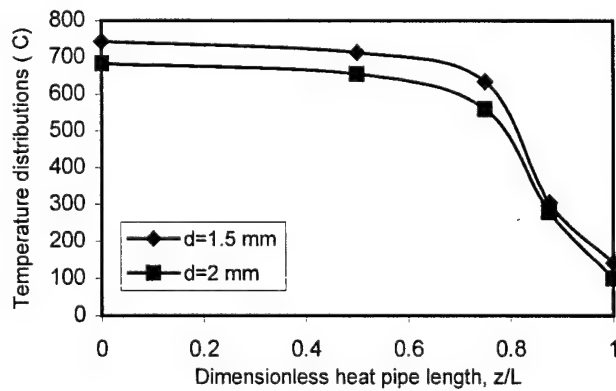
Fig. 4.14 Comparisons of temperature distributions along the dimensionless heat pipe length with the same flow rates of the cooling air.



(a) $Q=200 \text{ W}, \omega^2 \bar{Z}_a / g = 470$



(b) $Q=200 \text{ W}, \omega^2 \bar{Z}_a / g = 1306$



(c) $Q=200 \text{ W}, \omega^2 \bar{Z}_a / g = 1881$

Fig. 4.15 Comparisons of temperature distributions along the dimensionless heat pipe length with the same flow rates of the cooling air.

4.3 Comparisons of the Theoretical Predictions and Experimental Data for the Temperature Distributions along the Dimensionless Heat Pipe Length

According to the analyses in chapter 3, the non-condensable gases have an important influence on the temperature distributions along the heat pipe length. The analytical solution based on Eq. (3.7) predicts the temperature distributions along the heat pipe length without the diffuse effects of non-condensable gases. Eqs. (3.33), (3.34), and (3.35) give the closed-form analytical solution of temperature distributions along the heat pipe length with the diffuse effects of non-condensable gases. These analytical solutions for the temperature distributions are compared with the experimental results under the same geometrical dimensions and operating conditions of the heat pipes.

Table 4.2 and Fig. 4.16 show the comparisons among the analytical solutions without the diffuse effects of non-condensable gases, experimental data and the analytical solutions with the diffuse effects of non-condensable gases. It is clear that Eq. (3.7) gives a set of ideal analytical predictions without diffuse effects of non-condensable gases. In Eq. (3.7), the temperature distributions along the dimensionless heat pipe length are caused only by the friction on the liquid-vapor interface and the centrifugal force of the vapor. Therefore, at a higher operating temperature, the temperature drops along the dimensionless heat pipe length are very small, and the temperature distributions are approximately straight lines, as shown in Fig 4.16. The experimental results under the same conditions of operating conditions and geometrical dimensions are used in comparison with the analytical predictions. It can be seen that large discrepancies

between the analytical solutions from Eq. (3.7) and experimental results are present in the condenser sections, especially close to the condenser ends.

Eqs. (3.33), (3.34) and (3.35) give the temperature distributions along the dimensionless heat pipe length with the flat front of vapor-gas interface when the length occupied by non-condensable gases in the condenser section, $L_{c,n}$, is 4 mm. Compared to the closed-form analytical predictions and the experimental results in Table 4.2 and Fig. 4.16, it is evident that the analytical predictions from Eqs. (3.33), (3.34) and (3.35) are more realistic than the analytical predictions from Eq. (3.7) and are more close to the experimental results. According to Table 4.2 and Fig. 4.16, it can be found that the analytical solutions from Eqs. (3.33), (3.34) and (3.35) agree well with the experimental results in the entire evaporator section and most part of the condenser section. A larger deviation occurs only at the condenser end. This is because the condenser end cap for the tested heat pipe forms a huge heat sink since it is connected to the outer cylinder of the rotating experimental apparatus, and most of the heat from the end cap of the condenser is transferred into this heat sink when the heat pipe operates. As a result, the experimental data from the end cap of the condenser must be lower than the predictions from the closed-form analytical solution.

On the other hand, in practical cases, for the radially rotating miniature heat pipe, the vapor condenses on the inner wall of heat pipes, which forms a relatively low-pressure area on the inner wall of condenser section. The non-condensable gases in heat pipes tend to move toward the evaporator section under the action of the centrifugal force. Since the vapor pressure in the center of the cross-section is higher than that close to the inner wall, the non-condensable gases will diffuse along the low-pressure area

close to the inner wall. As a result, the vapor-gas interface between the vapor and non-condensable gases is not a flat front, but a spheroidal one, as shown in Fig. 4.17. This spheroidal vapor-gas interface will change the length of the non-condensable region, and affect the heat transfer and temperature distributions in the condenser section. Therefore, it may result in an additional deviation between the closed-form analytical predictions and experimental data in the condenser section.

Considering the complexities of the flow, heat transfer and geometry in the condenser section, Eqs. (3.33), (3.34) and (3.35) can still provide a good prediction for the temperature distributions along the heat pipe length.

Table 4.3 Comparisons of analytical solutions, experimental results and analytical solutions with the diffuse effects of non-condensable gases in the heat pipe ($L_{c,n} = 4$ mm).

(a) $\omega^2 \bar{Z}_a / g = 470$, $d_i = 1.5$ mm, $Q = 250$ W, $h_c = 226$ W/m²-°C

Dimensionless heat pipe length z/L	Analytical solution without non-condensable gas (°C)	Analytical solution with non-condensable gas (°C)	Experimental results (°C)
0.000	786.0	786.0	786.0
0.500	782.1	782.1	776.4
0.750	779.1	721.4	766.2
0.875	778.5	672.2	698.4
1.000	778.2	521.8	354.6

(b) $\omega^2 \bar{Z}_a / g = 470$, $d_i = 2$ mm, $Q = 280$ W, $h_c = 297$ W/m²-°C

Dimensionless heat pipe length z/L	Analytical solution without non-condensable gas (°C)	Analytical solution with non-condensable gas (°C)	Experimental results (°C)
0.000	830.0	830.0	830.0
0.500	828.6	828.6	821.8
0.750	827.6	764.3	804.4
0.875	827.3	711.9	742.4
1.000	827.2	551.4	390.0

(c) $\omega^2 \bar{Z}_a / g = 836$, $d_i = 1.5$ mm, $Q = 280$ W, $h_c = 326$ W/m²-°C

Dimensionless heat pipe length z/L	Analytical solution without non-condensable gas (°C)	Analytical solution with non-condensable gas (°C)	Experimental results (°C)
0.000	840.0	840.0	840.0
0.500	834.0	834.0	826.1
0.750	829.5	771.5	751.7
0.875	828.4	718.0	654.9
1.000	828.0	549.7	293.6

(d) $\omega^2 \bar{Z}_a / g = 836$, $d_i = 2$ mm, $Q = 280$ W, $h_c = 329$ W/m²-°C

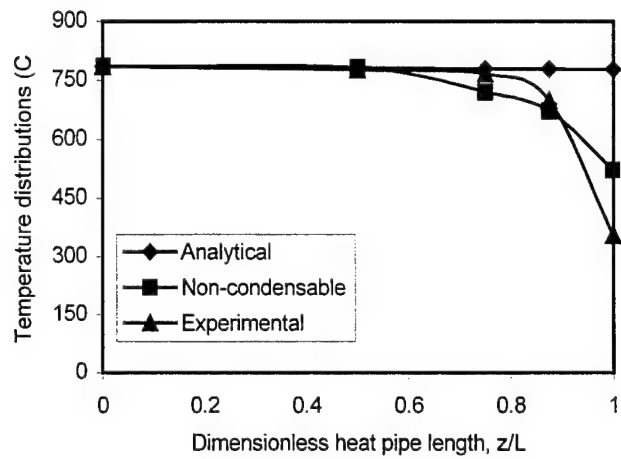
Dimensionless heat pipe length z/L	Analytical solution without non-condensable gas (°C)	Analytical solution with non-condensable gas (°C)	Experimental results (°C)
0.000	819.0	819.0	819.0
0.500	816.4	816.4	802.0
0.750	813.6	755.4	752.5
0.875	813.1	703.0	639.0
1.000	812.9	537.5	314.6

(e) $\omega^2 \bar{Z}_a / g = 1881$, $d_i = 1.5$ mm, $Q = 250$ W, $h_c = 336$ W/m²-°C

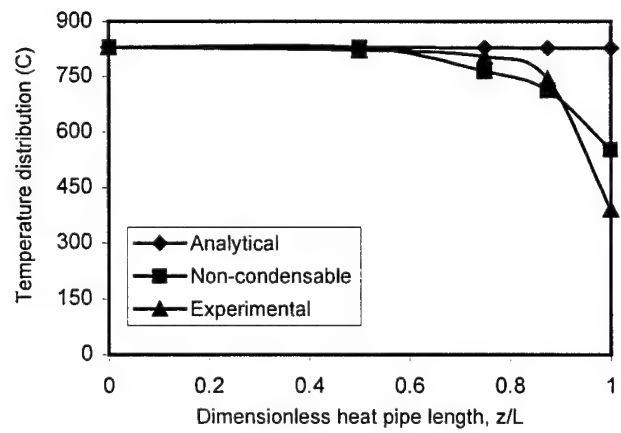
Dimensionless heat pipe length z/L	Analytical solution without non-condensable gas (°C)	Analytical solution with non-condensable gas (°C)	Experimental results (°C)
0.000	754.5	754.5	754.5
0.500	745.5	745.5	730.0
0.750	739.5	680.3	720.0
0.875	737.8	642.2	520.0
1.000	737.2	433.8	235.7

(f) $\omega^2 \bar{Z}_a / g = 1881$, $d_i = 2$ mm, $Q = 280$ W, $h_c = 392$ W/m²-°C

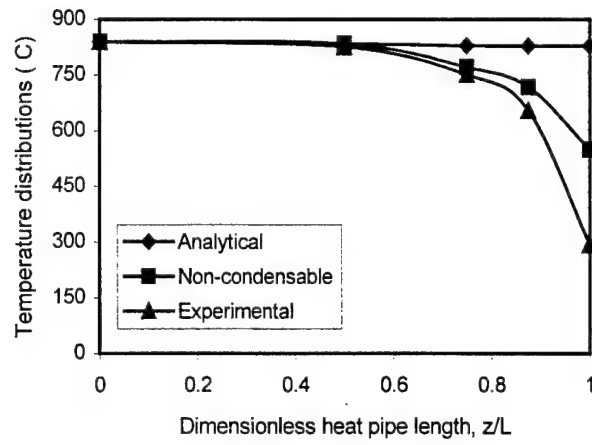
Dimensionless heat pipe length z/L	Analytical solution without non-condensable gas (°C)	Analytical solution with non-condensable gas (°C)	Experimental results (°C)
0.000	680.0	680.0	680.0
0.500	665.3	665.3	661.2
0.750	654.4	598.3	608.0
0.875	651.6	545.0	577.5
1.000	650.7	362.2	248.9



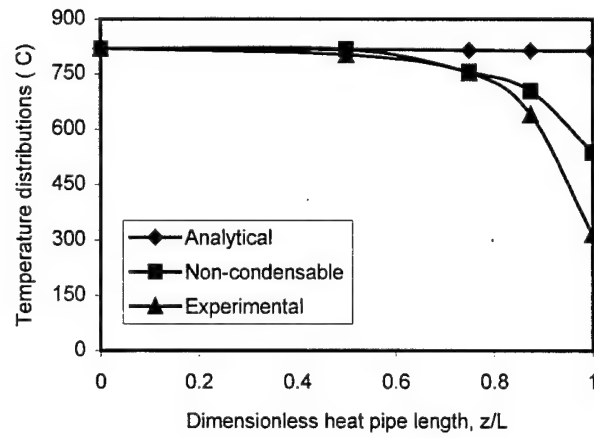
(a) $\omega^2 \bar{Z}_a / g = 470$, $d_i = 1.5$ mm, $Q = 250$ W



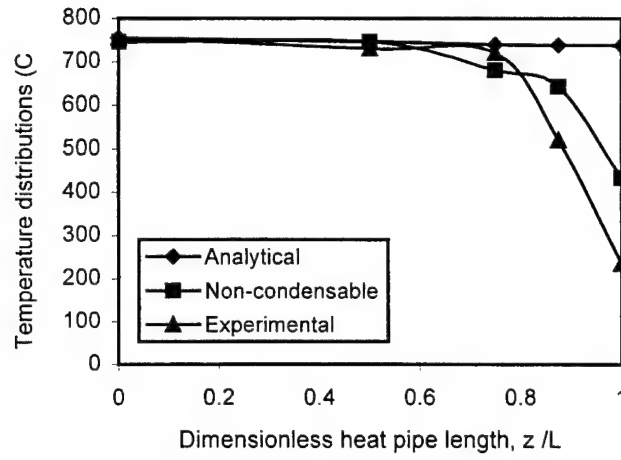
(b) $\omega^2 \bar{Z}_a / g = 470$, $d_i = 2$ mm, $Q = 280$ W



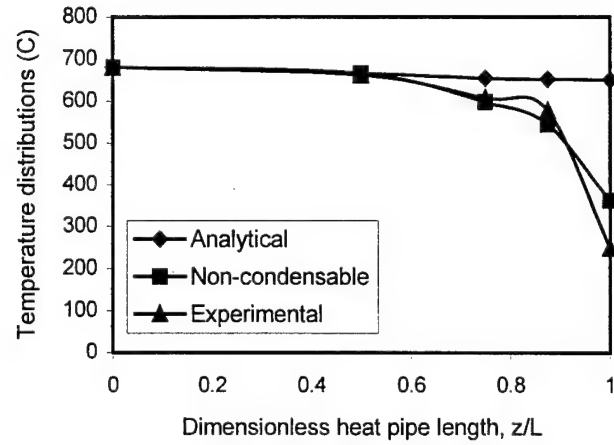
(c) $\omega^2 \bar{Z}_a / g = 836$, $d_i = 1.5$ mm, $Q = 280$ W



(d) $\omega^2 \bar{Z}_a / g = 836$, $d_i = 2$ mm, $Q = 280$ W



(e) $\omega^2 \bar{Z}_a / g = 1881$, $d_i = 1.5$ mm, $Q = 250$ W



(f) $\omega^2 \bar{Z}_a / g = 1881$, $d_i = 2$ mm, $Q = 275$ W

Fig. 4.16 Comparisons of analytical solutions, experimental results, and analytical solutions with the diffuse effects of non-condensable gases ($L_{c,n} = 4$ mm).

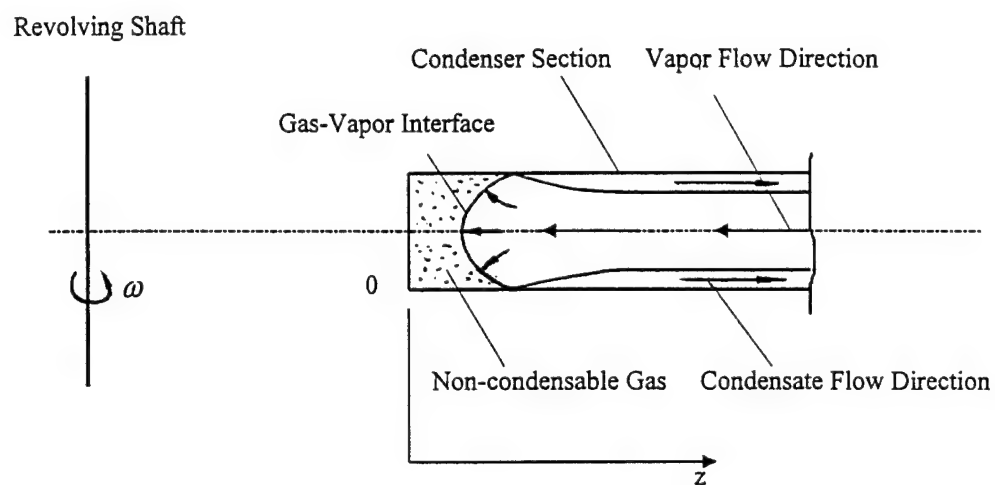


Fig. 4.17 Schematic of the diffuse effects of non-condensable gases at a higher revolution.

4.4 Error Analyses for Experimental Measurements and Analytical Solutions

Temperature distributions along the evaporator length exhibit a good agreement between the analytical solutions and experimental data. But significant deviations exist in the condenser section. The causes for these deviations are very complicated, and are relate to many influential factors. An error analysis is provided in this chapter, and the discrepancy between the analytical and experimental results may be attributable to the following factors:

1. The errors of experimental results, which include the uncertainties in the temperature and heat input measurements. In all experiments, the accuracy from the thermocouple of type K is 0.5%, the accuracy related to the slip ring which was used to transform the temperature signals is about 0.5%, and the HP34970 Data Acquisition has a temperature accuracy of about 0.2%. In addition, since it was difficult to weld the thermocouples onto the heat pipe shell, a high-temperature chemical cement was used to fix the thermocouples in the small holes drilled in the heat pipe shell. Therefore, it is possible to result in an error in the temperature measurement due to the contact thermal resistance between the thermocouples and the heat pipe shell at the measuring points. If the error caused by the contact thermal resistance is assumed to be 1%, the totally maximum uncertainty in the temperature measurement is about 2.2%. For the heat input measurement, the heater in the evaporator section is insulated with an insulation material of 16 mm in thickness stuffed between the heater and the heater cap in order to reduce the heat losses in the evaporator section. It was measured in experiments that the temperature on the outer surface of the heater cap was about between 40-45 °C , which corresponds to

a maximum heat loss of about 25 W when the highest temperature in the evaporator section was between 800-850 °C and the heat input was 250-300W. On the other hand, the maximum fluctuation range of the heat input in experiments was ± 2 W, which will result in an error of about 0.8% for the heat input. If the accuracy of the wattmeter and slip ring for the heat input is about 1.5%, the total uncertainty in the heat input is about 10%. As a result, the uncertainties in the temperature measurements along the heat pipe length and the heat input in the evaporator section contribute to the major sources of errors in experiments.

2. The errors of analytical solutions, which are caused by one-dimensional flow and heat transfer modeling. All analytical solutions are based on one-dimensional flow and heat transfer simplifications, while the flow and heat transfer in practical heat pipes should have three-dimensional characteristics, such as the spheroidal vapor-gas interface at the condenser section at a high rotating speed. Considering the miniature flow spaces and diameters in radially rotating miniature heat pipes and complexities of the flow and heat transfer, one-dimensional flow and heat transfer modeling should be sufficient to represent the major characteristics of the flow and heat transfer. However, the one-dimensional simplification will cause certain deviations between the analytical and experimental results.

3. The errors caused by experimental apparatus, which include the interference produced by the vibrations of experimental apparatus with high revolutions. In ideal cases, it is reasonable to treat the flow and heat transfer problems by a one-dimensional flow and heat transfer modeling due to the miniature flow spaces in radially rotating miniature heat pipes. But in practice, as the revolutions of the rotating apparatus was

increased, relatively large vibrations of the experimental apparatus were created. The one-dimensional flow and heat transfer in radially rotating miniature heat pipes will be interrupted in experiments due to the vibration of the experimental apparatus. As a result, it causes three-dimensional characteristics of the flow and heat transfer in experiments, which enhances the deviations between the analytical solutions and experimental results.

5. CONCLUSIONS AND RECOMMENDATIONS

5.1 Conclusions

The radially rotating miniature heat pipe is an effective heat transfer device, which uses the centrifugal force in the rotating heat pipe to return the condensate from the condenser section to the evaporator section.

In this report, an in-depth study for the radially rotating miniature heat pipe has been conducted both analytically and experimentally. The analytical solutions for the condensate film and vapor flows, film thickness, and temperature distributions along the heat pipe length are derived based on appropriate flow and heat transfer models. The diffuse effects of non-condensable gas on the temperature distribution along the heat pipe length are also studied. Extensive experimental tests on radially rotating miniature heat pipes with different influential parameters are conducted, and various effects on the operation of the heat pipes based on these influential parameters are searched. Analytical solutions for the temperature distributions along the heat pipe length with diffuse effects of non-condensable gases are obtained based on extensive experimental results. According to the analytical and experimental studies presented in this report, the following conclusions may be made:

1. The radially rotating miniature heat pipe has a simple structure, very low manufacturing cost, and very high heat transfer capability and effective thermal conductance (60-100 times higher than that of the copper). At the same time, the heat pipe can withstand strong vibrations, and work in the high-temperature and adverse

environments. Therefore, the combination of traditional air-cooling technology with radially rotating miniature heat pipes is a feasible and effective cooling means for high-temperature turboengine blades.

2. At a relatively high rotating speed or a large revolving radius, $\omega^2 \bar{Z} / g > 150$, the maximum temperature drop across the liquid film is negligible. However, a smaller heat pipe diameter or a lower heat pipe operating temperature may increase the temperature drop. Still, in any cases, the maximum temperature drop across the liquid film is much less than 1 K. It means that the commonly encountered condenser limitation for low temperature heat pipes would never be a serious problem for the high temperature heat pipes.

3. A heat pipe with sodium as the working fluid would have a smaller vapor temperature drop compared to the heat pipe with potassium as the working fluid. For the case without diffuse effects of non-condensable gases, the vapor temperature drop is on the order of 10-40 K. This temperature drop is relatively high for a low-temperature heat pipe. However, for the high-temperature heat pipes studied in this report, this temperature drop is small compared to the average heat pipe operating temperature level.

4. The inner diameter of the heat pipe determines the cross-section area of the vapor flow in the heat pipe. For a radially rotating miniature heat pipe with a larger inner diameter, the friction of the vapor flow is smaller. As a result, the temperature drop caused by the friction of the vapor flow is smaller. Conversely, a radially rotating miniature heat pipe with a smaller inner diameter would have a larger friction of the vapor flow that would cause a larger temperature drop along the heat pipe length. However, for a heat pipe with d_i/L greater than 0.02 or d_i greater than 1.5 mm, the

influence of the heat pipe diameter on the operating temperature level and the vapor temperature drop is relatively small.

5. The heat input has a very important influence on the temperature distributions and heat transfer characteristics of a heat pipe. When the flow rate of the cooling air, dimensionless centrifugal force, and inner diameters of the heat pipe are fixed, with an increase in heat input, the operating temperatures in the evaporator section will rise, the working section in the condenser will be increased, and the temperature level in the condenser section will go up. Accordingly, the heat transfer characteristics and effective thermal conductance will be improved greatly. However, a radially rotating miniature heat pipe with too high heat input will encounter its heat transfer limitation.

6. The dimensionless centrifugal force plays an important role in the temperature drop along the heat pipe. As the rotating speed of a heat pipe is increased, the dimensionless centrifugal force will rise, and the pressure and temperature drops along the heat pipes will increase accordingly. At a low rotating speed, the contribution of the centrifugal forces is relatively small, but at a high rotating speed, the contribution of the centrifugal forces becomes a dominant factor. This is especially obvious for a heat pipe having a relatively large diameter. However, at a fairly high rotating speed (15,000 rpm-20,000 rpm), the vapor temperature drop caused by the centrifugal force is still relatively small.

7. The flow rate of the cooling air in the condenser section has a dominant influence on the operating temperature of the heat pipe. When the flow rate of the cooling air is increased, the heat transfer capacity of the heat pipe will be improved, the operating

temperature of the heat pipe will be reduced, the working section of the condenser will be shorten, and the temperature distributions near the condenser end will become steeper.

8. The non-condensable gases in the heat pipe have an adverse effect on the operation of the heat pipe. The non-condensable gases will be driven to the condenser end by the vapor from the evaporator, and prevent the vapor to fill the entire condenser section. As a result, the non-condensable gases in the heat pipe will result in a large temperature drop near the condenser end and reduce the thermal conductance and heat transfer performance of the heat pipe.

5.2 Recommendations

1. The radially rotating miniature heat pipes can be made with different geometrical cross-sectional areas, such as square, triangular and elliptical cross-sectional areas in order to meet the requirement for various applications in industries.
2. Improving the performance of the rotating test apparatus, and conducting experiments for radially rotating miniature heat pipes at a higher rotating range that is close to the operating revolution of a gas turbine.
3. Seeking a better high-temperature chemical cement for the heater so that higher heat inputs can be provided in experiments.
4. Improving the filling procedure for radially rotating miniature heat pipes so that non-condensable gases can be eliminated in the heat pipe.

REFERENCES

- [1] Bathie, W. W., 1996, *Fundamentals of Gas Turbines*, John Wiley & Sons, Inc., New York, Chichester.
- [2] Bowman, W. J., 1987, "Simulated Heat Pipe Vapor Dynamics," Ph. D. Dissertation, Air Force Institute of Technology.
- [3] Cao, Y., 1996, "Rotating Micro/Miniature Heat Pipes for Turbine Blade Cooling Applications," *AFOSR Contractor and Grantee Meeting on Turbulence and Internal Flows*, Atlanta, GA.
- [4] Cao, Y., and Chang, W. S., 1997, "Analyses of heat transfer limitations of radially rotating heat pipe for turbomachinery applications," AIAA 97-2542, 32nd Thermophysics Conference, Atlanta, GA.
- [5] Cao, Y., Chang, W. S. and MacArthur, C. D., 1998, "An Analytical Study of Turbine Disk Incorporating Radially Rotating Heat Pipes," IMECE, Nov. 15-20, Anaheim, CA.
- [6] Cao, Y., Ling, J. and Chang, W. S. 1998, "Analyses of Liquid and Vapor Flows in a Miniature Radially Rotating Heat Pipe for Turbine Blade Cooling Application," 11th International heat and mass transfer conference, August, South Korea.
- [7] Chi, S. W., 1976, *Heat Pipe Theory and Practice: a Sourcebook*, Hemisphere Publishing Corporation, New York.
- [8] Cohen, H., Rogers, G. F. C. and Saravanamuttoo, H. I. H., 1994, *Gas Turbine Theory*, Longman Scientific & Technical, England.
- [9] Daniels, T. and Al-Jumaily, F., 1975, "Investigations of the Factors Affecting the Performance of a Rotating Heat Pipe," *Int. J. Heat Mass Transfer*, Vol. 18, pp. 961-973.
- [10] Dunn, P. D. and Reay, D. A., 1982, *Heat Pipe*, Pergamon Press, Oxford, New York.
- [11] Faghri, A., M. M. Chen and M. Morgan, 1989, "Heat Transfer in Two-Phase Closed Conventional and Concentric Annular Thermosphon," *ASME J. Heat Transfer*, Vol. 111, pp. 611-618.
- [12] Faghri, A., 1995, *Heat Pipe Science and Technology*, Taylor & Francis, Washington, DC.

- [13] Gray, V.H., 1969, "The Rotating Heat Pipe -- A Wickless, Hollow Shaft for Transferring Heat Fluxes," *Proc. ASME/AIChE Heat Transfer Conf.*, Minneapolis, pp. 1-5, ASME Paper No. 69-HT-19.
- [14] Harley, C. and Faghri, A., 1995, "Two-Dimensional Rotating Heat Pipe Analysis," *ASME J. Heat Transfer*, Vol. 117, No. 1, pp. 418-426. Harman, R. T. C., 1981, *Gas Turbine Engineering*, John Wiley & Sons, Inc., New York.
- [15] Ling, J., Cao, Y and Chang, W. S., 1999 "Analysis of Radially Rotating High-Temperature Heat Pipes for Turbomachinery Application," *ASME, Journal of engineering for gas turbines and power*, Vol. 121.
- [16] Maezawa, S., Suzuki, Y., and Tsuchida, A., 1981, "Heat Transfer Characteristics of Disk-Shaped Rotating, Wickless Heat Pipes," *Proc. 4th Int. Heat Pipe Conf.*, London, pp. 725-733.
- [17] Marto, P., 1976, "Performance Characteristics of Rotating Wickless Heat Pipes," *Proc. 2nd Int. Heat Pipe Conf.*, Bologna, pp. 281-291.
- [18] Nomoto, H., et al, 1997, "The Advanced Cooling Technology for the 1500 °C Class Gas Turbines: Steam-Cooled Vanes and Air-Cooled Blades," *ASME, J. of Engineering for Gas Turbines and Power*, Vol. 119, P624-632.
- [19] Norster, E. R., 1969, "*Combustion and Heat Transfer in Gas Turbine Systems*," Pergamon Press, Oxford, New York.
- [20] Peterson, G.P., 1994, *An Introduction to Heat Pipes*, John Wiley & Sons, Inc., New York.
- [21] Schumm, H. J., 1966, "Experimental Investigation of Two-Stage Air-Cooled Turbine Suitable for Flight at Mach 2.5," NASA TMX-148.
- [22] Shepherd, D. G. 1972, *Aerospace Propulsion*, American Eisevier Publishing, New York, London.
- [23] Suryanarayana, N. V., 1995, *Engineering Heat Transfer*, West Publishing Company, New York, Los Angeles.
- [24] Wagner, J. H., Johnson, B. V. and Hajek., T. J., 1991, "Heat Transfer in Passages with Smooth Walls and Radial Outward Flow," *ASME J. Heat Transfer*, Vol. 113, pp. 42-51.